

Development of a simulation model for the SuperNEMO tracker module

A thesis submitted to the University of Manchester for the degree of
Master of Science
in the Faculty of Engineering and Physical Sciences

2012

Daniel Leslie Hall

School of Physics and Astronomy

Contents

Abstract	6
Declaration	7
Acknowledgements	8
About the author	9
1 Introduction	10
2 Theoretical background	12
2.1 The neutrino in the Standard Model	12
2.2 The theory of double- β decay	15
2.3 Past and present experiments concerning double- β decay	17
2.4 The SuperNEMO experiment	18
3 The tracker module	22
3.1 Design of the SuperNEMO tracker	22
3.1.1 Design of an individual cell	23
3.2 The physics of a Geiger cell	24
3.2.1 The ionisation process	25
3.2.2 Drift of the electrons towards the anode	26

3.2.3	Plasma propagation and the cathode signal	31
3.2.4	The gas mixture	32
3.3	Reconstructing the particle's coordinates	33
3.3.1	Resolution of the reconstructed coordinate	37
4	Simulating the cell response	38
4.1	Simulating the cathode response	38
4.2	Simulating the anode response	42
4.2.1	The two-dimensional fit model	42
4.2.2	The timemap model	46
4.3	Resolution of the simulated drift time	52
4.4	Implementation into the simulation software	54
4.4.1	Structure of the simulation software SNWARE	55
4.4.2	Supplementary programs	56
5	Comparison of the models to experimental data	58
5.1	The SuperNEMO 18-cell module	58
5.2	Applying the models	60
5.3	Re-distributing the POCI	64
6	Conclusion	67

List of Figures

2.1	The particles in the Standard Model.	13
2.2	The three possible distributions for the neutrino masses.	14
2.3	Diagrams for (a) double- β decay with two neutrinos and (b) neutrinoless double- β decay.	16
2.4	The SuperNEMO demonstrator module.	18
2.5	The energy distribution expected in the presence of neutrinoless double- β decay.	20
3.1	Top down view of the SuperNEMO module used in the simulation.	23
3.2	(a) 3D view of an individual cell and (b) end-on schematic of a nine-cell array.	24
3.3	Plasma propagation along the cell.	31
3.4	An ideal event in the SuperNEMO cell.	35
4.1	Demonstrating cell recovery after an event.	41
4.2	A scatterplot of anode drift time against POCl.	43
4.3	Azimuthal dependence of parameters A and B.	45
4.4	The potential field in a SuperNEMO quarter cell.	47
4.5	The drift velocity to electric field relation.	48
4.6	The (a) timemap, (b) GARFIELD equivalent, (c) comparison of the two and (d) the two-dimensional fit.	51

4.7	Standard deviation of the Gaussians used to fit the distribution of drift times generated by GARFIELD.	54
4.8	The structure of the SNWARE software chain.	55
5.1	Simplified diagram of the 18-cell experimental setup.	59
5.2	Anode drift time distribution extracted from the 18-cell data.	61
5.3	Comparison of the drift time models against data from the 18-cell module.	63
5.4	The distribution of POCI in the cell, as given by (a) the SNWARE simulation and (b) the probability density functions on the x and y axes as given in Section 5.3	65
5.5	Comparison of the drift time models against data from the 18-cell module, using the re-distributed POCI	66

List of Tables

4.1	Definition of the event types in the Geiger cell.	40
-----	---	----

Abstract

SuperNEMO is an upcoming double- β decay experiment designed to search for the hypothetical process of neutrinoless double- β decay. It is composed of a double- β emitting isotope surrounded by a tracking volume. This tracking volume is in turn composed of an array of drift tubes operating in the Geiger mode. To provide an accurate simulation of the experiment, it is important to understand the movement of the electrons within each drift tube. In this study, the response of both the anode and cathode are considered. Two simulation models, called the timemap model and the two-dimensional fit model, have been developed to simulate the anode response. The timemap model is shown to be in good agreement with simulations made using the drift tube simulation software GARFIELD. The simulation models have been implemented as C++ packages that can be used as part of the SuperNEMO simulation. Both the models have been compared to data taken using a prototype module with 18 drift tubes.

Declaration

The author hereby declares that no portion of the work referred to in the thesis has been submitted in support of an application for another degree or qualification of this or any other university or other institute of learning.

1. The author of this thesis (including any appendices and/or schedules to this thesis) owns certain copyright or related rights in it (the “Copyright”) and s/he has given The University of Manchester certain rights to use such Copyright, including for administrative purposes.
2. Copies of this thesis, either in full or in extracts and whether in hard or electronic copy, may be made **only** in accordance with the Copyright, Designs and Patents Act 1988 (as amended) and regulations issued under it or, where appropriate, in accordance with licensing agreements which the University has from time to time. This page must form part of any such copies made.
3. The ownership of certain Copyright, patents, designs, trade marks and other intellectual property (the “Intellectual Property”) and any reproductions of copyright works in the thesis, for example graphs and tables (“Reproductions”), which may be described in this thesis, may not be owned by the author and may be owned by third parties. Such Intellectual Property and Reproductions cannot and must not be made available for use without the prior written permission of the owner(s) of the relevant Intellectual Property and/or Reproductions.
4. Further information on the conditions under which disclosure, publication and commercialisation of this thesis, the Copyright and any Intellectual Property and/or Reproductions described in it may take place is available in the University IP Policy (see <http://www.campus.manchester.ac.uk/medialibrary/policies/intellectual-property.pdf>), in any relevant Thesis restriction declarations deposited in the University Library, The University Library’s regulations (see <http://www.manchester.ac.uk/library/aboutus/regulations>) and in The University’s policy on presentation of Theses.

Acknowledgements

I would like to thank my supervisor Prof. Stefan Soldner-Rembold for his guidance during this project and for proof-reading the final version of this dissertation. I am also very grateful to Dr. David Urner for his support and guidance, and to Dr. Jo Pater for proof-reading this dissertation. My thanks also go to Ray Thompson, for answering all my questions regarding the Geiger cells and their construction. In particular, I would like to thank Dr. Emmanuel Chauveau for the patience it must have taken to share an office with me for ten months, as he tirelessly answered every question I had regarding the project. Last but not least, my thanks go to Prof. Fred Loebinger, for offering me a place on the MSc course, and to my parents, for their support and for financing me throughout my undergraduate and masters degrees and enabling me to benefit from a top-quality education.

About the author

Daniel Hall did his undergraduate MPhys at the University of Manchester, with an exchange year spent at the University of California Santa Barbara. He has worked as an undergraduate assistant to the Neutron Detector group at UCSB, and completed his MPhys research projects with the Nuclear Group and Accelerator Group at the University of Manchester.

Chapter 1

Introduction

SuperNEMO is an upcoming experiment designed to search for the hypothetical process of neutrinoless double- β decay. It consists of a source of double- β emitting isotope surrounded by a tracking volume. The tracking volume is capable of resolving the path of any charged particles that move through it, and is bounded by a calorimeter array that measures their energy. An important component of the experiment is its simulation software, which so far is capable of simulating the decay of a nucleus on the foil and the movement and capture of the resulting decay products, but does not simulate the physical response of the tracking volume, the calorimetry, or the electronics that are involved in reading out the data. It is important to have a complete simulation whose output is as similar as possible to that of the actual experiment, both to test analysis methods and to ensure the highest possible accuracy for an analysis Monte Carlo.

In this dissertation we will explain and test two simulation methods suitable for simulating the response of the tracker volume, given input data from the particle simulation. In Chapter 2 we will briefly summarise the theory of double- β decay and the various experiments that have been done in the field. We will also introduce the SuperNEMO experiment, its design and its capabilities. In Chapter 3 we will explain in more detail the design and physics of the tracker module.

In Chapter 4 we will introduce and explain the simulation methods that have been developed as part of this study. We will examine their accuracy and computational efficiency, as well as how they compare to similar third-party simulation software. In Chapter 5 we will test the simulation methods against data. Finally, in Chapter 6 we will draw conclusions as to the reliability of the simulation models and whether they are suitable for use in the SuperNEMO simulation software.

Chapter 2

Theoretical background

2.1 The neutrino in the Standard Model

The neutrino is a light, neutral, weakly-interacting subatomic particle first proposed by Wolfgang Pauli in 1930 to explain how the process of single β -decay is able to conserve the overall energy, momentum and spin of the process [1]. Pauli initially named the particle the neutron, although the discovery in 1932 by James Chadwick of the more massive particle today known by that name led Enrico Fermi to rename Pauli’s postulated particle the *neutrino*, meaning “little neutral one”. Fermi’s theory of β -decay, and by extension the neutrino, was initially met with some skepticism - however, the direct observation of the neutrino in 1956 [2] confirmed the existence of the particle.

Initially believed to be one particle, it is now known that three distinct flavours of neutrino exist, each one related to one of the three generations of leptons in the Standard Model: electron, muon and tau. Each neutrino carries one unit of lepton number – said unit being negative in the case of an anti-neutrino – meaning that in the β -decay process

$$n \rightarrow p + e^- + \bar{\nu}_e \tag{2.1}$$

Three generations of matter (fermions)				
	I	II	III	
mass →	2.4 MeV/c ²	1.27 GeV/c ²	171.2 GeV/c ²	0
charge →	$\frac{2}{3}$	$\frac{2}{3}$	$\frac{2}{3}$	0
spin →	$\frac{1}{2}$	$\frac{1}{2}$	$\frac{1}{2}$	1
name →	u up	c charm	t top	γ photon
Quarks	4.8 MeV/c ²	104 MeV/c ²	4.2 GeV/c ²	0
	$-\frac{1}{3}$	$-\frac{1}{3}$	$-\frac{1}{3}$	0
	$\frac{1}{2}$	$\frac{1}{2}$	$\frac{1}{2}$	1
	d down	s strange	b bottom	g gluon
Leptons	<2.05 eV/c ²	<0.17 MeV/c ²	<18.2 MeV/c ²	91.2 GeV/c ²
	0	0	0	0
	$\frac{1}{2}$	$\frac{1}{2}$	$\frac{1}{2}$	1
	ν_e electron neutrino	ν_μ muon neutrino	ν_τ tau neutrino	Z⁰ Z boson
	0.511 MeV/c ²	105.7 MeV/c ²	1.777 GeV/c ²	80.4 GeV/c ²
	-1	-1	-1	± 1
	$\frac{1}{2}$	$\frac{1}{2}$	$\frac{1}{2}$	1
	e electron	μ muon	τ tau	W[±] W boson
				Gauge bosons

Figure 2.1: The three generations of quarks, leptons and gauge bosons in the Standard Model [3, 4].

the overall lepton number is conserved. Nowadays, the neutrinos take their place in the Standard Model as shown in Figure 2.1.

The electron neutrino has an upper mass limit of $m_{\nu_e} < 2.05 \text{ eV}/c^2$ [4], whilst the limits on the masses of the muon and tau neutrino are considerably higher, $m_{\nu_\mu} < 0.17 \text{ MeV}/c^2$ and $m_{\nu_\tau} < 18.2 \text{ MeV}/c^2$, respectively. Despite only the upper limit being known, the neutrinos are proven to have mass due to the phenomenon of neutrino oscillations. The effects of this were first observed in the Homestake Mine experiment in the 1960s, and later measured directly by the Super-Kamiokande [5], SNO [6] and KamLAND [7] experiments. The oscillations arise from the fact that the weak (flavour) eigenstates of the neutrinos are not equal to their mass eigenstates, but that these are instead related via the Pontecorvo-Maki-Nakagawa-Sakata (PMNS) matrix. The two separate sets of eigenstates are related via the unitary transformation

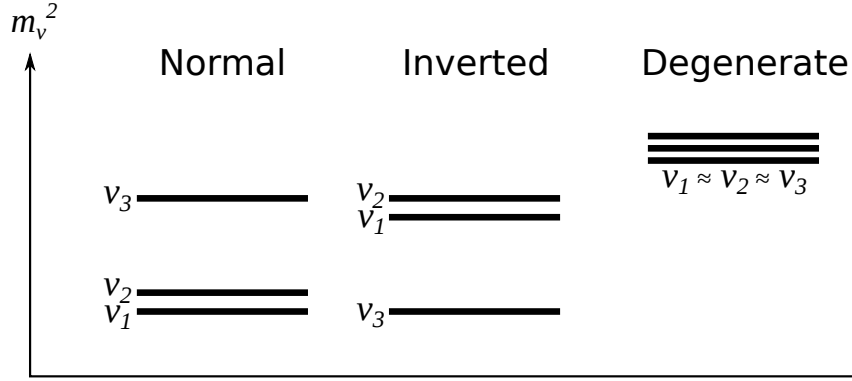


Figure 2.2: The three possible distributions for the neutrino masses.

$$|\nu_\alpha\rangle = \sum_{i=1}^3 U_{\alpha i} |\nu_i\rangle \quad , \quad (2.2)$$

where the indices α and i denote the flavour and mass eigenstates, respectively, and U is the PMNS neutrino mixing matrix.

The mass of the neutrino remains unknown, as do many details regarding its nature as a particle. The Standard Model allows for the neutrino to be a Dirac or Majorana particle (or some mixture of both, in the see-saw mechanism). A Dirac particle is defined such that its particle wavefunction $|\nu\rangle$ is not equal to its antiparticle wavefunction $|\bar{\nu}\rangle$, i.e. its charge conjugate. The reverse is true for a Majorana particle, meaning that the particle is its own antiparticle. All evidence collected to date has not provided any indication as to whether neutrinos are pure Dirac or Majorana particles or some mixture of the two. Of further interest is the mass hierarchy of the three neutrino flavours, and whether these follow a normal, inverted or quasi-degenerate structure as illustrated in Figure 2.2. These remain open questions in particle physics that can be investigated via the process of double- β decay.

2.2 The theory of double- β decay

Double- β decay was first proposed by Goeppert-Mayer in 1935 [8] and observed by Inghram and Reynolds in 1950 [9]. The process describes a transition from a nucleus of mass number A and atomic number Z to a nucleus of atomic number $Z + 2$,

$$(A, Z) \rightarrow (A, Z + 2) + 2e^- + 2\bar{\nu}_e , \quad (2.3)$$

via the emission of two electrons and two anti-neutrinos as seen in Figure 2.3 (a). The process has a half-life on the order of 10^{20} years [10], and as such single β -decay is always favoured when it is allowed. To study the process through experiment, β -decay must be strongly suppressed, either through conservation of energy or orbital angular momentum.

Most observable double- β decays occur between even-even nuclei, and require that the mass of the mother nucleus, $m(A, Z)$, be greater than the mass of the daughter nucleus, $m(A, Z + 2)$, and (for the practical purposes of forbidding standard β -decay) less than the mass of the intermediate nucleus, $m(A, Z + 1)$. The pairing effects present between nucleons in an even-even nucleus grant the latter an increased binding energy compared to even-odd and odd-odd nuclei, and this forbids standard β -decay in many even-even nuclei. An exception to this is ^{48}Ca , where standard β -decay is allowed by conservation of energy but not by conservation of angular momentum, meaning that β -decay is a first forbidden process and hence strongly suppressed. Because of this, it is possible to observe double- β decay in ^{48}Ca .

The half-life of standard double- β decay, $T_{1/2}^{2\nu}$, is given by the relation [11]

$$(T_{1/2}^{2\nu})^{-1} = G^{2\nu} |M^{2\nu}|^2 , \quad (2.4)$$

where $G^{2\nu}$ is the phase space factor and $M^{2\nu}$ is the nuclear matrix element. This form of double- β decay has been observed in 12 different nuclei [12, 13, 14].

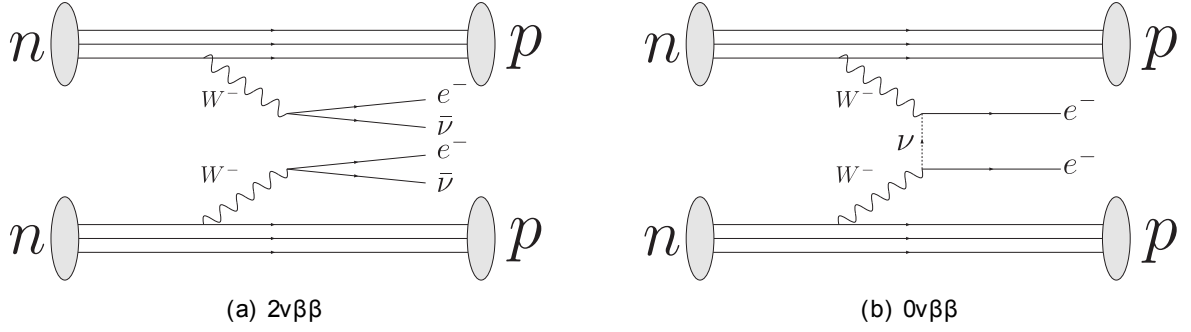


Figure 2.3: Diagrams for (a) double- β decay with two neutrinos and (b) neutrinoless double- β decay.

An alternative form of the process, proposed in 1939 by Furry [15], is neutrinoless double- β ($0\nu\beta\beta$) decay. This is described by the transition

$$(A, Z) \rightarrow (A, Z + 2) + 2e^- , \quad (2.5)$$

where the W bosons interact via the exchange of a virtual neutrino, as illustrated in Figure 2.3 (b). This process violates the conservation of lepton number. For this to occur, the neutrino must be its own antiparticle - a requirement only fulfilled if the neutrino is a Majorana particle. In contrast to the half-life described in Equation 2.4, the half-life of this process is sensitive to the effective neutrino mass $\langle m_{\beta\beta} \rangle$ [11] :

$$(T_{1/2}^{0\nu})^{-1} = G^{0\nu} |M^{0\nu}|^2 \langle m_{\beta\beta} \rangle . \quad (2.6)$$

The effective neutrino mass is related to the PMNS matrix and is defined as

$$\langle m_{\beta\beta} \rangle = \sum_{i=1}^3 m_i U_{ei}^2 , \quad (2.7)$$

where e denotes the electron components of the matrix.

The observation of neutrinoless double- β decay would mark a significant leap forward in the understanding of particle physics; a half-life for the process would place a lower limit

on the neutrino mass and provide some indication as to the mass hierarchy of the three neutrino flavours. The process has not yet been observed, and it remains the focus of a number of experiments.

2.3 Past and present experiments concerning double- β decay

To date a number of experiments have been conducted with the intent of proving or ruling out the existence of neutrinoless double- β decay, employing a number of different approaches. In general, these experiments have followed two schools of thought:

- **Source = Detector:** Experiments where the detector material is also the $\beta\beta$ source. Examples include the IGEX [16], Heidelberg-Moscow [17], Cuoricino [18], GERDA [19] and CUORE [20] experiments.
- **Source \neq Detector:** Experiments where the $\beta\beta$ source is placed near a separate detector array. Examples are the NEMO and ELEGANTS [21] series of experiments.

The NEMO series of experiments includes the now decommissioned NEMO3 (for which NEMO and NEMO2 were prototypes) and the upcoming SuperNEMO experiment – the one of interest to this study. The NEMO3 experiment [22] ran from 2003 to 2011, investigating double- β decay in seven separate isotopes : ^{100}Mo , ^{82}Se , ^{116}Cd , ^{150}Nd , ^{96}Zr , ^{48}Ca and Te , both in its natural form and as enriched ^{130}Te . So far neutrinoless double- β decay has not been observed in the collected data, and recent results have placed a lower limit on the half-life of [23, 24] :

$T_{1/2}^{0\nu}$	Isotope	C.L.	$\langle\nu_{\beta\beta}\rangle$	Exposure
$> 4.6 \times 10^{23} \text{ y}$	^{100}Mo	90%	$< 0.7 - 2.8 \text{ eV}$	7368.6 g·y
$> 1.8 \times 10^{22} \text{ y}$	^{150}Nd	90%	$< 4.0 - 6.3 \text{ eV}$	92.5 g·y
$> 1.0 \times 10^{23} \text{ y}$	^{82}Se	90%	$< 1.7 - 4.9 \text{ eV}$	993.3 g·y

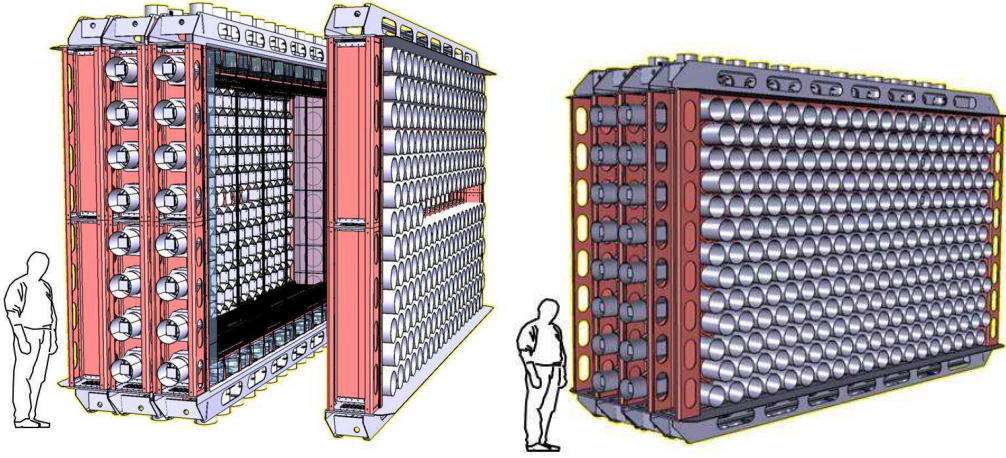


Figure 2.4: The SuperNEMO demonstrator module. The source foil (not shown) lies at the centre of a tracking volume, which is enclosed within an array of calorimeters (in grey). The support structure is shown in red. Image from reference [28].

Concurrent to NEMO3 was the Heidelberg-Moscow experiment, which originally placed a lower limit on the half-life $T_{1/2}^{0\nu} > 1.9 \times 10^{25}$ years [25]. A re-evaluation of the data by a sub-group of the collaboration claimed an observation of $0\nu\beta\beta$ events, with an associated half-life of $T_{1/2}^{0\nu} = (0.8 - 18.3) \times 10^{25}$ years [26]; however, this claim remains strongly disputed [27]. Regardless of the accuracy of such a claim, it is well within the means for investigation by future experiments such as CUORE and SuperNEMO.

2.4 The SuperNEMO experiment

The SuperNEMO experiment is the successor to the now-dismantled NEMO3 experiment, and like its predecessor is a source \neq detector experiment. A single source foil of a double- β isotope is surrounded on either side by an array of charged particle trackers and calorimeter blocks. The design of a single module is illustrated in Figure 2.4; the completed SuperNEMO experiment will consist of 20 such modules installed in the Laboratoire Souterrain de Modane. A single demonstrator module is currently under construction for both the purposes of physics and as a test-bed for the final experiment.

The particle tracking system is an array of drift tubes operating in the Geiger mode, and is described in detail in the next chapter. Mounted on either side of the tracking volume is an array of modular calorimeters, each unit consisting of a scintillator block attached to a photomultiplier tube. A similar array of calorimeters is mounted above and below the source foil to serve as a gamma veto. The entire module lies within a uniform magnetic field that serves to deflect the path of charged particles through the tracking volume. This is the primary advantage of SuperNEMO over other double- β experiments: with data from the tracking volume, the event reconstruction software can reliably determine the origin of a $\beta\beta$ event and so remove the majority of background events not originating from the source foil. The curvature of the path of the charged particles through the magnetic field is also used to distinguish positrons from electrons.

A double- β decay in SuperNEMO (neutrinoless or not) will be marked by the emission of two electrons that will leave a path through the tracker and be absorbed by the calorimeters. This is isolated from background events (passing electrons, other decays, spallations, etc.) by imposing the following requirements:

1. An event consists of exactly two separate tracks and two separate calorimeter hits.
2. The curvature of the two tracks must both correspond to that expected of an electron moving through the detector.
3. Each of the two tracks must begin on the source foil and end at one of the two calorimeters that fired.
4. The two tracks must share a common vertex on the source foil.
5. The probability that the event is internal (i.e. originated from the source foil) must be greater than 4% and the probability that it is external (i.e. an event crossing the detector) must be less than 1%. This is determined from the particle time-of-flight that is extrapolated from the calorimeter hit times.

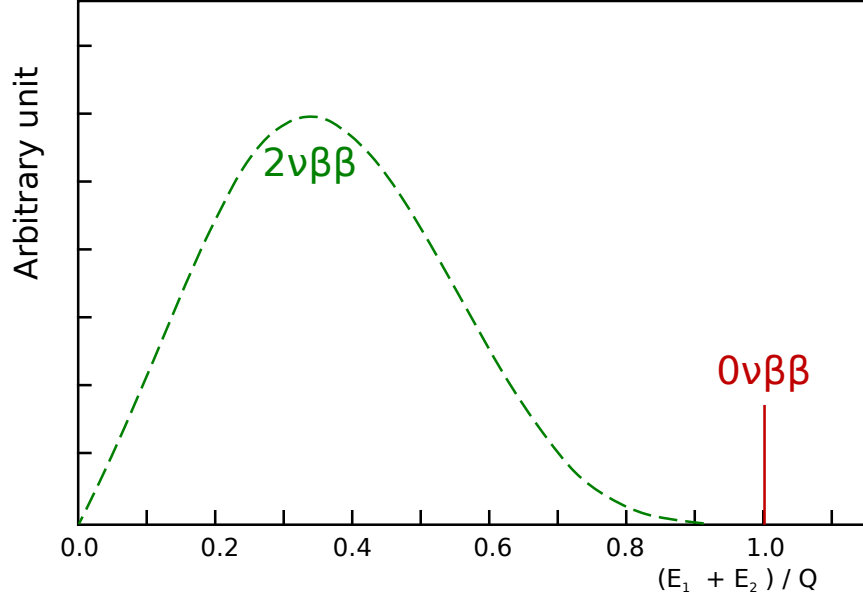


Figure 2.5: The energy distribution expected in the presence of both two-neutrino and neutrinoless double- β decay. The $\beta\beta 0\nu$ peak has been highly exaggerated for visibility.

6. No other tracks (prompt or delayed) must be present.
7. No photons must be present. These are indicated by a calorimeter hit with no associated track.

The presence of double- β decay is indicated by the presence of a peak at the high end of the energy distribution of the two electrons produced in the decay. Since in $0\nu\beta\beta$ decay no neutrinos are emitted, the sum of the energies of the two electrons, E_1 and E_2 , will be equal to the Q -value of the decay. An exaggerated example of an energy distribution where both $2\nu\beta\beta$ and $0\nu\beta\beta$ are present is shown in Figure 2.5.

The major advantage of SuperNEMO is that it is background-free; the background for the demonstrator module in the region of interest is expected to be < 0.06 events per year. Another important advantage is that SuperNEMO is capable of reconstructing the angle between two electrons emitted in a double- β event. If neutrinoless double- β decay is observed, this variable provides a tool to investigate the underlying interaction mechanism.

The completed SuperNEMO experiment will be sensitive to a $0\nu\beta\beta$ half-life of $T_{1/2}^{0\nu} = 1.2 \times 10^{26}$ years [28], corresponding to a neutrino mass sensitivity of ≈ 70 meV. Many details regarding the final design of the experiment, including the composition of the source foil, are still under debate.

Chapter 3

The tracker module

The SuperNEMO tracker is composed of two arrays of drift tubes – referred to as Geiger cells – operating in the Geiger mode, placed on either side of the source foil. In this chapter we will introduce the design of an individual cell, and discuss the physics that determines the cell’s response to a charged particle.

A drift tube design was chosen for two reasons: firstly, they are more cost effective per unit volume than solid-state trackers – an advantage that is further enhanced by operating them in the Geiger mode as opposed to the proportional mode. Secondly, the anode and cathode signals from a Geiger cell are on the order of 200 and 30 mV respectively and do not necessitate an amplifier directly connected to the cell. This latter advantage is especially important since it minimises the amount of electronics located near the sensitive volumes of the experiment, thus improving the design’s radiopurity. A high degree of radiopurity is essential in keeping the background as low as possible.

3.1 Design of the SuperNEMO tracker

The two arrays of Geiger cells are each 9 cells deep and 114 cells wide, with the readout electronics located on top of the module and connected via a feed-through to the individual

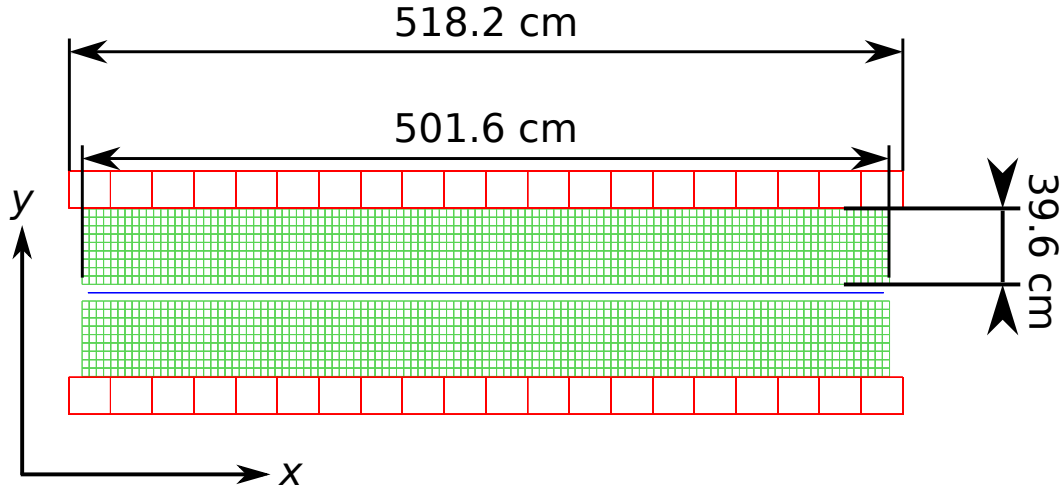


Figure 3.1: Top down view of the SuperNEMO tracker geometry as used in the SNWARE simulation. The source foil is shown in blue and the calorimeter blocks in red. The Geiger cells are shown in green, and each cell is drawn as a square.

anodes and cathodes of each cell. Each array is 270 cm tall by 501.6 cm wide by 39.6 cm deep, and begins 34 mm from the source foil. Located just beyond the tracker arrays are the two arrays of calorimeter blocks that serve to measure the energy of the traversing particles. A top-down view of the tracker as used in the simulation is shown in Figure 3.1.

3.1.1 Design of an individual cell

Each cell in the tracker array is constructed from 12 guard wires, 1 anode wire and 2 delrin end caps that each contain a copper cathode ring. Both the cathode rings and guard wires are grounded, whilst the anode wire is kept at a specified operating voltage. The guard wires are shared with the cell's neighbours and are held taut by the two end caps mounted into the tracker frame. The anode wire runs through the centre of the cell and cathode rings. The design of a single SuperNEMO cell is shown in Figure 3.2 (a) and an end-on schematic of a nine cell array is shown in figure 3.2 (b). In prototype tests the readout signal is taken from both of the cathodes and the anode. In the demonstrator module and the final experiment there will no readout taken from the lower cathode, thus reducing the

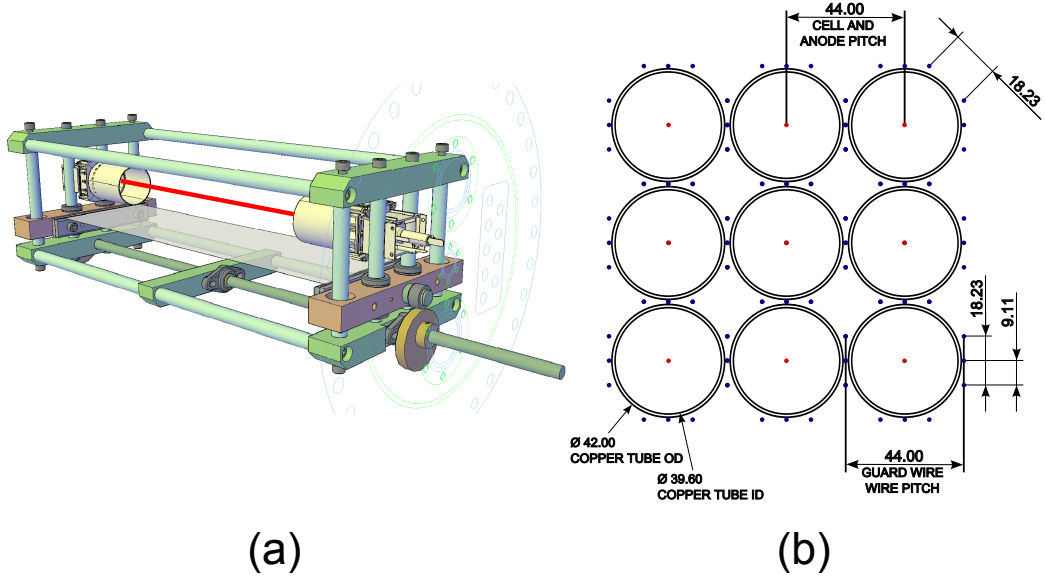


Figure 3.2: Simplified diagram of the a) side view and b) end-on view of a single SuperNEMO cell. The anode wire is shown in red and the guard wires in black. The cathode rings are shown in blue; the dashed cathode is only present in the prototype cells, and will not be used in the demonstrator module. The dashed rectangles indicate the location of the cell endcaps.

amount of readout electronics by a third.

3.2 The physics of a Geiger cell

A Geiger cell is a gaseous drift tube detector operating in the Geiger mode, as opposed to the more standard proportional mode. A charged particle moving through the cell ionises the gas mixture, creating clusters of electron-ion pairs along its path. In the presence of the electric field generated by the anode wire, the electrons begin to drift towards it; conversely, the ions begin to drift towards the guard wires, although this drift is far slower by comparison. When the electrons reach the anode a signal is detected; in the proportional mode, the strength of this signal is proportional to the energy deposited by the ionising particle. This is not the case in the Geiger mode. In this section we shall demonstrate how the physics of this mode allows us to reconstruct both the radial and longitudinal

coordinate of the particle, although we can no longer determine the energy deposited by the particle. Geiger cells also suffer from a comparatively long dead time following an event – approximately 3-6 ms – although for the NEMO3 and SuperNEMO experiments, with a trigger rate of about 0.05 Hz per cell, this does not present a problem.

3.2.1 The ionisation process

A fast electron moving through the gas in the cell creates clusters of electron-ion pairs along its path. In the simplest case, we consider a homogeneous isotropic gas in which the likelihood of an ionisation occurring is independent of position. We define the mean free path of this traversing particle between such ionising collisions to be [29]

$$\lambda = \frac{1}{N\sigma_i} , \quad (3.1)$$

where N and σ_i are the electron density and ionisation cross-section of the gas, respectively. The mean number of ionising collisions that occur over a length L is $\langle k \rangle = L/\lambda$, with a frequency described by a Poisson distribution. Thus, the probability that a number of k such ionising collisions occur along a length L is [29]

$$P(L/\lambda, k) = \frac{(L/\lambda)^k}{k!} e^{-L/\lambda} . \quad (3.2)$$

An alternative approach is to consider the energy deposited by the particle. When a traversing particle loses an amount of energy ΔE in a gas whose ionisation potential is δE , the average number of ionisation pairs created is [30]

$$\langle k \rangle = \frac{\Delta E}{\delta E} . \quad (3.3)$$

As in the case of Equation 3.2, the frequency is described by a Poisson distribution

$$P(\delta E/\Delta E, k) = \frac{(\Delta E/\delta E)^k}{k!} e^{-\Delta E/\delta E} . \quad (3.4)$$

To simulate the ionisation generated by a traversing particle, we begin by taking the path of the particle through the cell and extracting its length, L , and the amount of energy deposited in the cell, ΔE . These variables are given by the underlying particle simulation, in this case GEANT4 [31]. We now sample a value at random from the Poisson distribution given in Equation 3.4 to obtain the number of ionisation clusters generated by the traversing particle. Following this, we use a uniform probability distribution to randomly place these clusters along the path. Once this distribution is generated, we simulate the drift of the electrons towards the anode wire that results in the anode signal.

3.2.2 Drift of the electrons towards the anode

Since the ion drift does not contribute to the cell's signal, we shall only concern ourselves with the drift of the electrons produced in the ionisation process. The study of electron drift in gaseous mixtures is a rich topic that has evolved from its simple description derived from the classical kinetic theory of gases to a much more extensive description using non-equilibrium statistical mechanics, with much of this progress having been made over the last half-century [32]. In this section we shall introduce the more transparent classical, macroscopic picture before briefly summarising the much more intricate picture painted by the solutions to the Boltzmann transport equation.

In the macroscopic theory derived from the classical model of gases, electrons in a gas possess a Maxwellian energy distribution with a mean value kT , where k is the Boltzmann constant and T the temperature of the gas. Under the influence of an electric field \mathbf{E} and a magnetic field \mathbf{B} , these electrons gain a net drift velocity \mathbf{u} . The equation of motion for these electrons thus becomes [29]

$$m \frac{d\mathbf{u}}{dt} = e\mathbf{E} + e[\mathbf{u} \times \mathbf{B}] - K\mathbf{u} , \quad (3.5)$$

where e is the charge of the electron, m its mass, and K is a friction term due to interactions with the gas. We define a characteristic time,

$$\tau = \frac{m}{K} , \quad (3.6)$$

as the mean time between collisions of electrons with molecules in the gas. We consider the case $t \gg \tau$, resulting in the steady state solution to Equation 3.5 for which $d\mathbf{u}/dt = 0$. The drift velocity vector is thus described by the linear equation

$$\frac{\mathbf{u}}{\tau} - \frac{e}{m} [\mathbf{u} \times \mathbf{B}] = \frac{e}{m} \mathbf{E} \quad (3.7)$$

To solve for the drift velocity we make the substitutions $(e/m)B_\mu = \omega_\mu$, $(e/m)E_\mu = \epsilon_\mu$, where $\mu = x, y, z$ and $\omega^2 = \sum_\mu \omega_\mu^2$, and express Equation 3.7 in the matrix form

$$M\mathbf{u} = \epsilon , \text{ where} \quad (3.8)$$

$$M = \begin{bmatrix} 1/\tau & -\omega_z & \omega_y \\ \omega_z & 1/\tau & -\omega_x \\ -\omega_y & \omega_x & 1/\tau \end{bmatrix} ,$$

and for which the solution is obtained by inverting M . An alternative form for this solution is

$$\mathbf{u} = \frac{e}{m} \tau |\mathbf{E}| \frac{1}{1 + \omega^2 \tau^2} \left(\hat{\mathbf{E}} + \omega \tau [\hat{\mathbf{E}} \times \hat{\mathbf{B}}] + \omega^2 \tau^2 (\hat{\mathbf{E}} \cdot \hat{\mathbf{B}}) \hat{\mathbf{B}} \right) , \quad (3.9)$$

where $\hat{\mathbf{E}}$ and $\hat{\mathbf{B}}$ are the unit vectors in the direction of the electric and magnetic fields, respectively. In the absence of a magnetic field $\omega \tau = 0$, and Equation 3.9 reduces to [29, 32]

$$\mathbf{u} = \frac{e}{m}\tau \mathbf{E} = \mu \mathbf{E} , \quad (3.10)$$

where $\mu = e\tau/m$ denotes the scalar mobility. For non-zero magnetic fields, the mobility μ becomes a tensor given by $(e/m)M^{-1}$.

In the SuperNEMO experiment a uniform magnetic field is present throughout the tracker volume. When considering a cross-section of the cell perpendicular to the anode wire, the magnetic field is orthogonal to the electric field at most points in the cell, i.e. $\mathbf{E} \cdot \mathbf{B} = 0$. Although this does not apply in the proximity of the cathodes, this feature is important when considering the effect of the magnetic field upon the drift of the electrons towards the anode.

We define our x - y plane to be perpendicular to the anode wire and centred upon a drifting electron, with the positive x -axis defined as being in the direction of the electric field currently experienced by the electron. In this frame of reference, $\mathbf{E} = (E_x, 0, 0)$ and $\mathbf{B} = (0, 0, B_z)$; Equation 3.9 thus reduces to three components for \mathbf{u} :

$$\begin{aligned} u_x &= \frac{(e/m)\tau}{1 + \omega^2\tau^2} |\mathbf{E}| , \\ u_y &= \frac{(e/m)\tau}{1 + \omega^2\tau^2} \omega\tau |\mathbf{E}| , \text{ and} \\ u_z &= 0 . \end{aligned} \quad (3.11)$$

The tangent of the angle ψ between the x and y components of \mathbf{u} is defined as

$$\tan \psi \equiv \frac{u_y}{u_x} = -\omega\tau , \quad (3.12)$$

and thus the magnitude of \mathbf{u} is given by

$$|\mathbf{u}| = \frac{(e/m)\tau}{\sqrt{1 + \omega^2\tau^2}} |\mathbf{E}| = \frac{e}{m}\tau |\mathbf{E}| \cos \psi \quad (3.13)$$

and its direction by

$$\hat{\mathbf{u}} = \frac{\hat{\mathbf{E}} + \omega\tau \left[\hat{\mathbf{E}} \times \hat{\mathbf{B}} \right]}{\left| \hat{\mathbf{E}} + \omega\tau \left[\hat{\mathbf{E}} \times \hat{\mathbf{B}} \right] \right|} . \quad (3.14)$$

The product $|\mathbf{E}| \cos \psi$ is the component of the electric field in the direction of the drift velocity. This relation implies that the functional dependence of $|\mathbf{u}|$ on $|\mathbf{E}|$ and $|\mathbf{B}|$ is

$$|\mathbf{u}| = F(E, B) = F(E \cos \psi, 0) , \quad (3.15)$$

a result known as Tonk's theorem [29, 33]. The result of this functional dependence is that independent of the direction of the electron drift, the magnitude of $|\mathbf{u}|$ is determined by the component of the electric field in the drift direction for any magnetic field, provided that $\mathbf{E} \cdot \mathbf{B} = 0$ and that τ is constant [29]. This result has been verified experimentally for fields up to 12 kG [29].

Another aspect of the electron drift is diffusion; as the electron cluster travels towards the anode it will spread according to a diffusion coefficient D . The mechanics of this diffusion process is described in reference [29]. In the classical limit the distribution of an electron cluster along a direction x , beginning point-like at a time $t = 0$, is described by a Gaussian distribution with a standard deviation

$$\sigma_x^2 = 2Dt , \quad (3.16)$$

where D is a field-dependent diffusion coefficient. Until 1967 it was always assumed that the diffusion of the cluster was isotropic, until work by Wagner et al [34] demonstrated otherwise: the diffusion coefficient along the electric field varies substantially from that perpendicular to it. As the electric field increases – and with it, the average energy of the electrons – the ratio $D_L/D_T < 1$, where D_L and D_T are the coefficients for diffusion parallel and perpendicular to the electric field [29]. This means that the electron cluster

is described by two separate Gaussian distributions, the wider of the two describing the spread transverse to the drift direction – an effect known as electron anisotropy. The description just given relies on there being no magnetic field present; if this is not the case, the more complicated effect of magnetic anisotropy manifests itself, at which point the diffusion coefficient is represented by a 3×3 tensor.

The classical theory relies upon the electron energy distribution remaining Maxwellian under the influence of an electric field. While this may hold for some gases such as carbon dioxide (a so-called “cool” gas), electric fields of only a few V / cm in Argon are enough to considerably increase the average electron energy [32]. This is accounted for by the comparatively more accurate microscopic theory, which relates to the cross-sections of the molecules in the gas mixture. The microscopic theory usually relies either upon finding solutions to the Boltzmann transport equation [35] or Monte Carlo simulations of the movement of individual electrons in the gas mixture at the microscopic level [36]. Some drift simulation programs such as MAGBOLTZ [37] use a mixture of both methods. The classical theory is also not able to account for electron or magnetic anisotropy. Hence, in this study we shall rely upon the classical theory when it is appropriate to do so, apart from in the calculation of drift velocities and diffusion coefficients, which will be handled by MAGBOLTZ.

In a SuperNEMO cell, the geometry is such that a free electron anywhere in the cell should ultimately be drawn to the anode wire by the electric field, with the drift velocity being greater the closer the electron is to the wire. Hence, when the electron-ion clusters are formed along the path of the particle through the cell, it is the cluster closest to the wire that will be responsible for the start of the anode signal. The signal is proportional to the rate at which charge is collected by the wire; when there are no more free electrons remaining, the signal stops. The location of the nearest electron cluster to the wire is known as the point of closest ionisation – hereafter referred to as the POCI – and is ultimately what is resolved from the coordinate reconstruction. The fact that the POCI does not

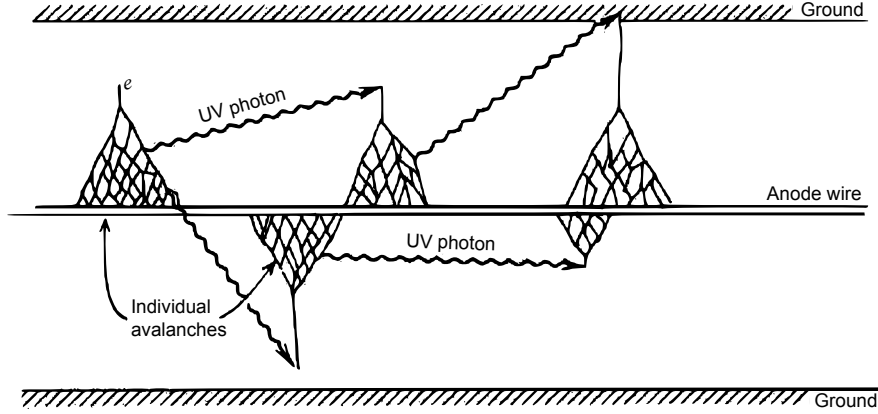


Figure 3.3: Plasma propagation along the cell in the Geiger mode. The avalanche process that occurs in the proximity of the wire (here shown in exaggerated scale) emits UV photons that travel to nearby regions of the cell. These trigger further ionisations in the un-fired regions of the cell either side of the original avalanche.

necessarily correspond to the point of closest approach between the traversing particle and the anode wire accounts in part for the resolution of the cell.

3.2.3 Plasma propagation and the cathode signal

As the electrons approach the wire they ionise the gas in their path, producing more electron-ion pairs in proportion to the strength of the local electric field. In a cell design such as that used in SuperNEMO the electric field increases strongly in the region close to the wire, which results in the drifting electrons generating a Townsend avalanche in the proximity of the wire. This is illustrated in Figure 3.3.

The energy of the electrons in the Townsend avalanche is such that bremsstrahlung results in the emission of ultraviolet (UV) photons. These photons travel a short distance before ionising the gas elsewhere in the proximity of the anode wire. Since region of the cell where the original avalanche occurred has already been ionised, this ionisation occurs a short distance either side of this region. This leads to a knock-on effect whereupon this UV ionisation generates further Townsend avalanches and in turn more UV photons, each

time affecting the non-ionised region adjacent to the previous avalanche. The result is a positively charged plasma that propagates lengthways down the cell, forming a sheath around the anode wire. This propagation continues either until the plasma reaches the cathodes at either end.

Studies in NEMO3 [22] have shown that the speed with which the plasma propagates longitudinally down the cell is approximately constant, until it reaches the ends of the cell and enters the cathode ring. When the plasma enters the cathode ring, the sudden depletion of electrons generates a positive electric field, which in turn induces a negative charge on the inside of the cathode rings. To neutralise the field generated by the positive plasma, electrons are drawn from the ground, generating a potential drop between the ground and the cathode; this potential is detected by the electronics as a signal to which a timestamp is applied. In section 3.3 we will demonstrate how the anode and cathode signal can be used to reconstruct the radial and longitudinal coordinate of the traversing particle.

3.2.4 The gas mixture

The gas mixture in a NEMO3 cell is He-4 (95%), Ar-18 (1%) and Ethyl alcohol (4%) – percentages are quoted by volume. Helium was chosen as the major gas in the mixture due to being unreactive and of low atomic number, thus reducing the amount of energy deposited by the traversing particle. Argon was added to the mixture after studies [22] demonstrated that it improved the stability of the longitudinal plasma propagation, as well as reducing problems associated with cell ageing.

The SuperNEMO gas mixture is expected to be identical to that used in NEMO3, although ongoing studies in which the argon is replaced with neon have shown promising preliminary results [38, 39]. During this study the two gas mixtures that were used for the experiment were the standard NEMO3 mixture and helium/neon/alcohol in the volume

ratio of 94/2/4 percent.

The Ethyl alcohol serves as a quenching gas, whose purpose is to prevent double-firing of the cell due to the He/Ar/Ne ions creating secondary electron-ion pairs upon reaching the guard wires. When these ions are neutralised by the guard wires, there is a small likelihood that the process will generate further electrons. These will then drift towards the anode and generate a false signal. The quenching gas has a lower ionisation energy than Helium, Argon and Neon, and when these drifting ions collide with the Ethyl molecules the Ethyl molecules neutralise the He/Ar/Ne ions. The resulting Ethyl ions then drift towards the guard wire, with the final outcome being that the ions arriving at the guard wire are those of the quenching gas. The more complicated molecular structure of the Ethyl alcohol inhibits the creation of secondary electron-ion pairs and greatly decreases the probability of a false signal.

3.3 Reconstructing the particle's coordinates

The ideal output of a SuperNEMO prototype cell is shown in Figure 3.4 – the two major differences between this and the true SuperNEMO cell is that in Figure 3.4 two cathodes signals are present as opposed to one, and no calorimeter signal is present. The data extracted from this event are four measurements: the time the anode signal begins, t_{anode} , the time the first (negative) peak on the anode derivative signal begins, t_{deriv} , and the times of the first and second cathode peaks, t_{c1} and t_{c2} , respectively. These last two can also be extracted from the anode derivative signal by searching for two neighbouring peaks, the first being negative and the second being positive. An example of this two-peak feature in the derivative signal can be seen at points B and C in Figure 3.4. However, to resolve the left/right ambiguity during coordinate reconstruction at least one cathode signal must be present.

All the important features of a cell event are present in Figure 3.4. The anode signal

begins and increases to a maximum as the rate of electron collection becomes constant; this signal then halves when the plasma reaches one of the cathodes. The sudden spike in the anode signal immediately before the drop is due to the difference in the electric field experienced by the electrons within the cathode ring. The cathode rings are grounded but of a smaller radius than the side length of the cell, hence the electric field within the cathode ring is greater. When the gas within the ring is ionised, the electrons drift towards the anode faster than those generated in the main body of the cell, resulting in a short spike in the signal. This effect is seen at points B and C in Figure 3.4 and is responsible for the two-peak features on the derivative signal. Once the plasma has reached both ends of the cell the gas in the proximity of the wire has been completely ionised, and the anode signal drops to below the original voltage as the remaining positive ions counteract the potential field generated by the anode wire. The anode signal steadily increases back to the original value as the ions neutralise on the guard wires.

The anode signal does not actually lie at 0 mV due to readout requirements. Hence, a constant value referred to as the *pedestal* is subtracted from the data. This is obtained by taking the integral of the anode voltage in the early region of the event window, and dividing said integral by the difference between its limits. If the cell had not completely recovered or if a signal is present in the beginning of the window – where no signal should be present, since the triggered signal should begin at a predefined time in the window – then the pedestal value will differ from that of an ideal event. This allows a requirement to be applied during analysis to isolate only those events with a pedestal value close to the ideal, removing a number of bad events in which the cell may still be recovering.

A further important time is that of the associated calorimeter array, t_{calo} . In the timescale of the electron drift from the POCI to the wire, the electron time-of-flight from the cell to the calorimeter is negligible – hence, t_{calo} is taken to be the time that the POCI is generated. From this, we take the drift time from the POCI to the anode wire to be $t_{drift} = t_{anode} - t_{calo}$. The anode derivative time is used as a consistency check, since ideally

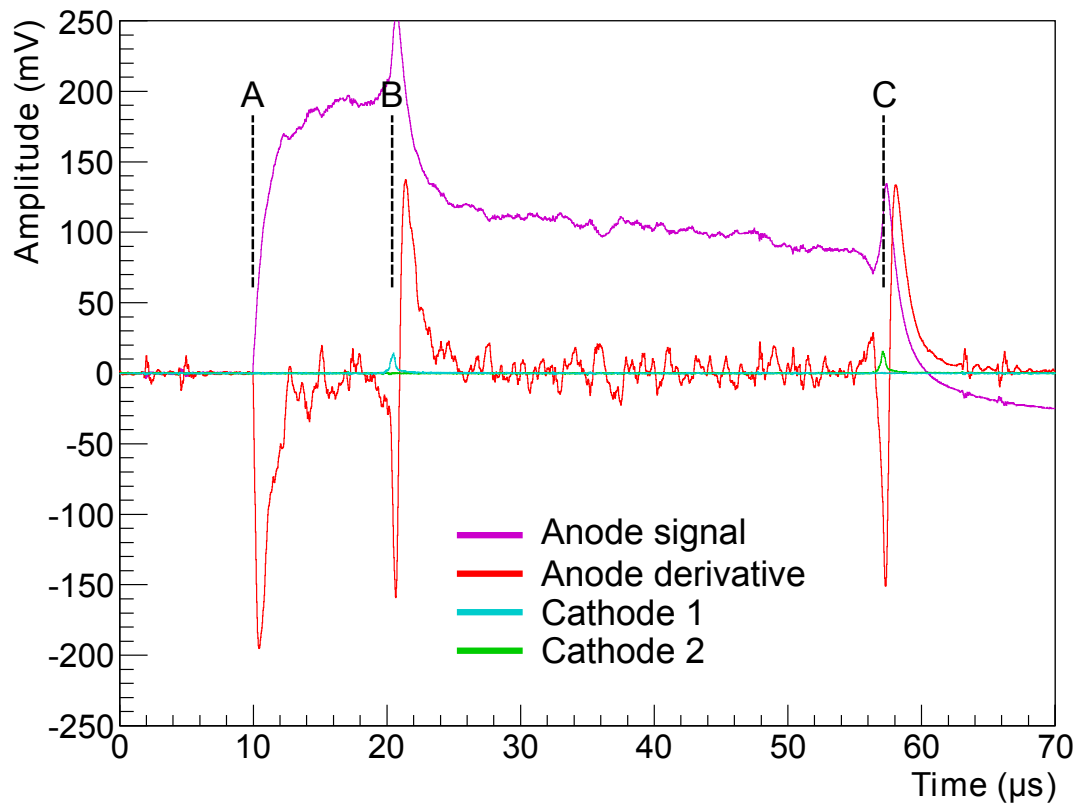


Figure 3.4: A typical event in the prototype cell, with both cathodes operating. The anode charge collection begins at point A, and the plasma reaches cathodes 1 and 2 at points B and C, respectively.

$$t_{anode} \approx t_{deriv}.$$

From these five times it is possible to reconstruct the longitudinal and radial coordinate of the point of closest ionisation (POCI) to the anode wire. We consider the cylindrical coordinate system $\mathbf{r} = (r, \theta, z)$, where the z -axis is along the anode wire (with $z = 0$ halfway down the cell) and the (r, θ) plane is perpendicular to and centred at the anode wire. The coordinate $\mathbf{r} = (0, \theta, 0)$ corresponds to a point lying at the centre of the anode wire halfway along the cell. We define Cathode 1 as lying in the region $z < 0$ and Cathode 2 at $z > 0$.

The z -coordinate is determined from the cathode times t_{c1} and t_{c2} , via the relation [22]

$$z = \frac{L_{eff}}{2} \frac{t_{c2} - t_{c1}}{t_{c2} + t_{c1}} \left[1 - K \frac{L_{eff}}{2} \left(1 - \left| \frac{t_{c2} - t_{c1}}{t_{c2} + t_{c1}} \right| \right) \right], \quad (3.17)$$

where L_{eff} is the effective length of the cell in mm, the distance along the z -axis from the edge of Cathode 1 to the edge of Cathode 2, and $K = 0.408 \times 10^{-4} \text{ (mm)}^{-1}$ is a constant. The first-order component is that which assumes a constant plasma propagation speed along the cell. The second component accounts for the reduced plasma propagation speed that is due to a decrease in the high voltage during propagation. This last term is dependent upon the voltage on the anode and the gas mixture, and the value of K quoted is that used in NEMO3.

The anode reconstruction can be done through two sets of relations. For NEMO3, first analyses were done using the following equations [40]:

$$r = \begin{cases} 0.025 & t_{drift} = 0 \\ (0.598 + 0.0045t_{drift}) & 0 < t_{drift} < 60 \\ (-0.292 + 0.023t_{drift}) & 60 < t_{drift} < 220 \\ (0.22t_{drift}^{0.572}) & 220 < t_{drift} < 1480 \\ 14.3 & t_{drift} \geq 1480 \end{cases} \quad (3.18)$$

with the radius r given in mm and t_{drift} in ns. Subsequent analyses have used a single relation

$$r = \frac{6.759t_{drift}}{t_{drift}^{0.84} + 287.09} + 0.1877 , \quad (3.19)$$

although this relation does not so well apply for anode times of $t_{drift} < 60$ ns, for which the old relation is used.

3.3.1 Resolution of the reconstructed coordinate

In NEMO3, the resolution on the radial (i.e. transverse) and longitudinal coordinate are considered separately. The transverse resolution is given by the relation [22]

$$\sigma_{\perp} = \sqrt{\sigma_{int}^2 + k \left(\frac{\sqrt{L_{track}}}{E} \right)^2} , \quad (3.20)$$

where $\sigma_{int} = (0.37 \pm 0.02)$ mm is the intrinsic radial resolution, L_{track} is the length of the particle's path through the cell, E is the initial energy in keV of the particle when it entered the cell, and $k = (10.8 \pm 1.7)$ mm keV² is a fitting constant. The values quoted are those used in the NEMO3 analyses.

The longitudinal resolution follows a similar relation that is dependent upon the longitudinal coordinate [22] ,

$$\sigma_{\parallel} = \sigma_0 \sqrt{1 - \left(\frac{2z}{L_{eff}} \right)^2} , \quad (3.21)$$

where L_{eff} is the effective length of the cell and $\sigma_0 \approx 1.1$ cm is the maximum resolution on the longitudinal coordinate possible for a POCI at the mid-length of the cell.

Chapter 4

Simulating the cell response

To achieve an effective simulation of the experiment, it is important that the response of each individual Geiger cell is modelled correctly to obtain a realistic set of anode and cathode times. The response of each cell is divided into three stages: the ionisation process, the drift of the electrons towards the anode, and the propagation of the plasma towards the cathodes, occurring in that order. In this chapter we shall first discuss the cathode simulation as it was done in NEMO3 and conclude as to whether any modifications are necessary. We shall then two separate models that can be used to simulate the drift of the electrons from the POCI to the anode wire, and compare them to established third-party software. Finally, we will briefly explain how the simulation of an individual cell is incorporated into the overarching simulation of the entire experiment.

4.1 Simulating the cathode response

As discussed previously, the cathodes require the plasma to propagate from the location of the first Townsend avalanche to the inside of the cathode ring for a signal to be generated. Data [41] taken with an 18-cell module using cosmic ray muons shows that the plasma propagation efficiency is higher than 99%, provided that there is no dust on the anode

wire. The presence of dust at a location on the wire inhibits plasma propagation beyond this point and can reduce this efficiency to as low as 30%.

Studies in NEMO3 have shown that the plasma propagation speed is approximately constant, as implied in the (quasi-)linear relation seen in Equation 3.17. In the NEMO3 simulation, the cathode time simulation is done assuming a linear relationship between longitudinal position and time (i.e. Equation 3.17 with $K = 0$) and a constant plasma velocity. Given the longitudinal coordinate of a POCl, the cathode times are given by

$$\begin{aligned} t_{c1}^{(N3)} &= \frac{L_{eff} + 2z}{2v} \quad \text{and} \\ t_{c2}^{(N3)} &= \frac{L_{eff} - 2z}{2v} , \end{aligned} \tag{4.1}$$

where z is the longitudinal coordinate, L_{eff} the effective length of the cell and v the velocity of the plasma. The cathode times $t_{c1}^{(N3)}$ and $t_{c2}^{(N3)}$ are explicitly those times given by the NEMO3 simulation, and represent the time it takes for the plasma to propagate from a point z along the wire to their respective cathode. Since the plasma does not start to propagate until the first avalanche begins this means that

$$\begin{aligned} t_{c1} &= t_{drift} + t_{c1}^{(N3)} \quad \text{and} \\ t_{c2} &= t_{drift} + t_{c2}^{(N3)} . \end{aligned} \tag{4.2}$$

However, the NEMO3 simulation does not simulate the electron drift, so there is no value of t_{drift} present to offset the cathode times to their realistic values.

A constant plasma velocity implies a constant plasma propagation time, i.e. that $t_{c1} + t_{c2} \approx \text{constant}$ for all events. However, data taken with a single SuperNEMO cell triggering on cosmic ray muons [41] shows that the plasma propagation time is actually a function of both the time since the last event in the cell – the *event delay* – and the nature of this previous event. We define the nature of the event in one of three ways according to its cathode signal, as given in table 4.1. As seen in Figure 4.1 (a), the plasma propagation time increases exponentially for event delays of less than 5 ms, and far more

Event type	Description
Full	Both cathodes in the event have a signal with amplitude over 5 mV
Partial	Only one cathode in the event has a signal above 5 mV
No cathode	Neither cathode has a signal above 5 mV

Table 4.1: *Definition of event types in the Geiger cell.*

non-full events are seen at short event delays. This implies that the plasma propagation is hindered by the recovery of the cell; as fewer non-ionised particles are present in the cell, the probability that a UV photon generated during a Townsend avalanche causes further ionisation down the cell is decreased. This results in a slower propagation velocity with a greater chance that the propagation will halt before reaching the cathode. The lower number of non-ionised particles also results in a reduced amplitude on the anode signal, as seen in Figure 4.1 (b).

It appears that the cell is capable of recovering comparatively faster from partial events. This can be seen in Figure 4.1 (a) where full events succeeding a partial one demonstrate shorter plasma times than those succeeding a full one of a similar event delay. However, since during these events the cell is recovering in a non-homogeneous manner, the plasma propagation velocity may not be constant along the length of the cell.

However, event rates in SuperNEMO are expected to be ≈ 0.05 Hz per cell, and so it is highly unlikely that the effects of cell recovery will be observed in the data. Furthermore, the reconstruction of the longitudinal coordinate relies on the ratio of the two cathodes times and not on the absolute value of the propagation time, nor on the offset presented by t_{drift} in Equation 4.2. Therefore we can conclude that it is not necessary to amend the cathode simulation model used in NEMO3 for use in SuperNEMO, although the inclusion of the drift time offset is recommended.

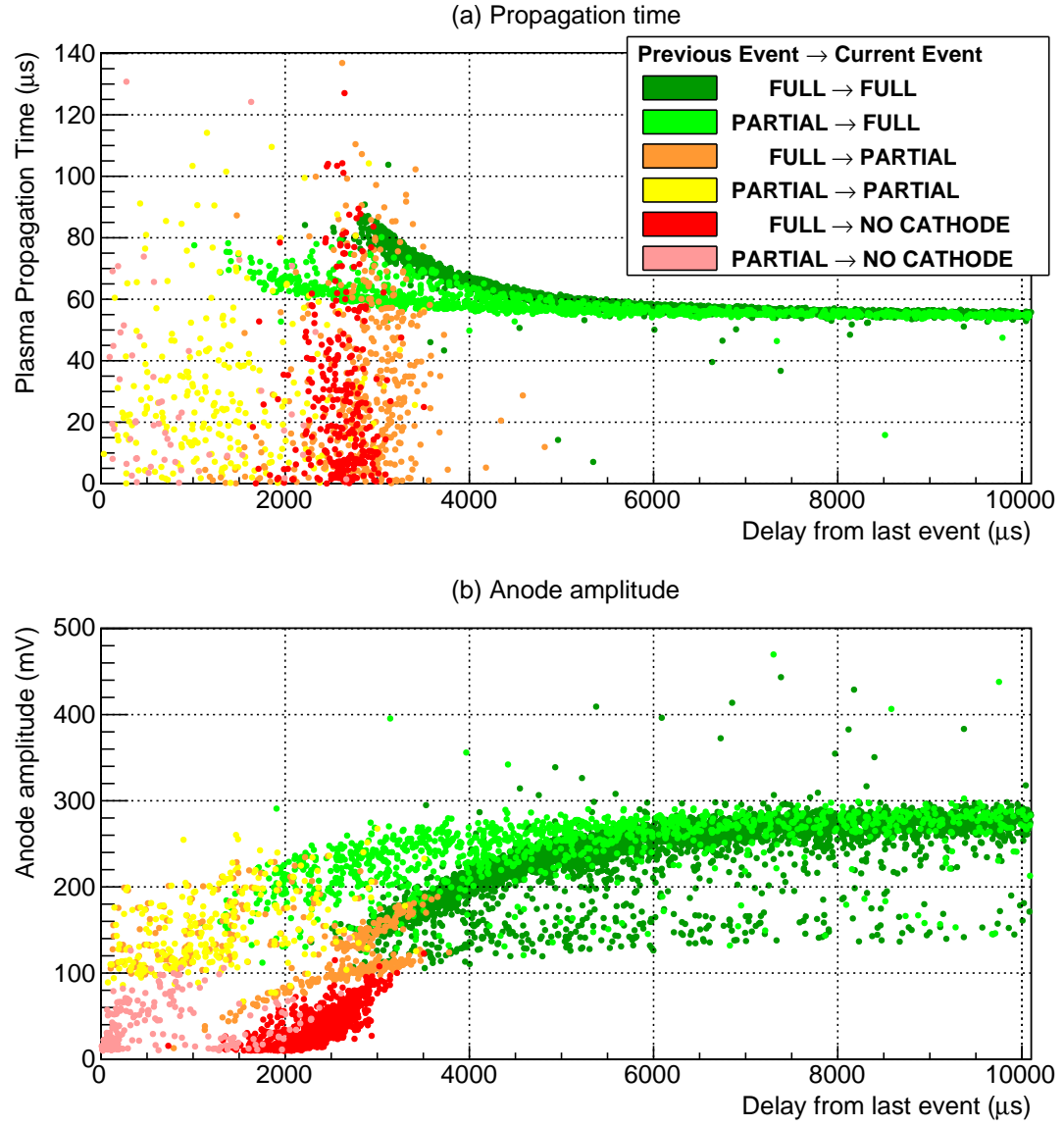


Figure 4.1: Demonstrating cell recovery. The event delay time is the time since the last event triggered in the cell. The legend indicates both the type of the current event and the one preceding it. The event type is defined in Table 4.1

4.2 Simulating the anode response

As mentioned in section 4.1, the NEMO3 simulation does not simulate the drift of the electrons from the POCI and the resulting anode signal; instead the distance of the POCI from the anode wire is given directly, bypassing the need to reconstruct the radial coordinate in the manner described in section 3.3. In SuperNEMO it is necessary to simulate the electron drift and extract a realistic drift time for two reasons: firstly so that the simulation output better matches that of the actual experiment, and secondly so that the effectiveness of the reconstruction methods can be tested against the simulation.

In this section we will describe two separate methods that can be used to simulate the electron drift in the Geiger cell. The first, referred to as the two-dimensional fit model, involves simulating the cell in GARFIELD [42] and modelling the electron drift, developing a one-to-one functional form between the POCI and the drift time. The second approach is to develop a C++ module for the simulation software capable of solving for the electric potential in the cell and simulating the electron drift directly. The latter is referred to as the timemap model, and is benchmarked against results given by GARFIELD [42].

4.2.1 The two-dimensional fit model

In the two-dimensional fit model we find a functional form that describes the relationship between the coordinate of the POCI in the plane of the cell and the resulting anode drift time. We use the simulation program GARFIELD to simulate the drift of an electron toward the anode wire from a point in the cell. Repeating this process multiple times for points distributed randomly throughout the plane of the cell, we construct a two-dimensional distribution of drift time as a function of position. We then develop a two-dimensional fit for this distribution.

We consider a cross-section of a single SuperNEMO cell, with the x - y plane perpendicular to the anode and guard wires. GARFIELD is capable of solving Poisson's equation

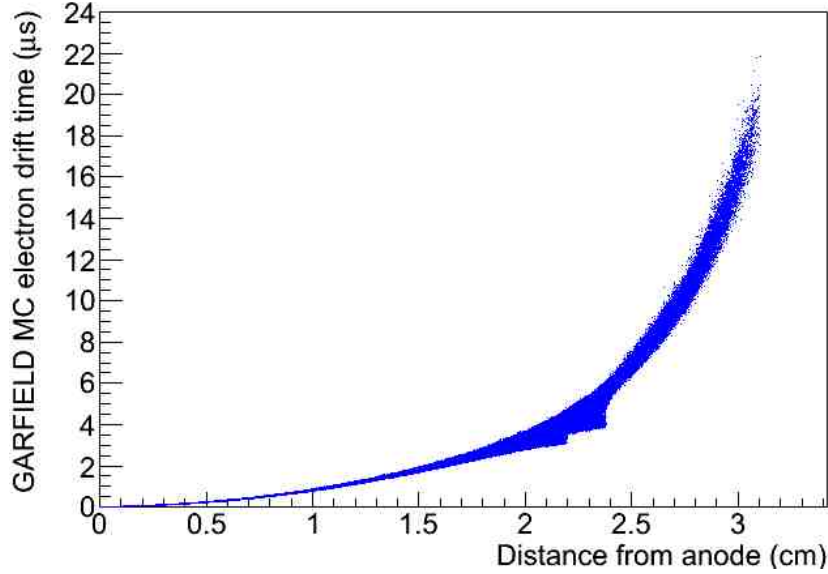


Figure 4.2: A scatterplot of anode drift time against POCI. Generated using GARFIELD’s *MC_electron_drift* function call.

for the cell and, via an interface with the MAGBOLTZ program, simulating the drift of an electron from a point (x, y) to its collection on the anode wire. GARFIELD has three function calls for this purpose: Microscopic, Runge-Kutta and Monte Carlo. The Microscopic function utilises the Monte Carlo microscopic theory mentioned in section 3.2.2, and whilst being the most accurate of the three is only computationally efficient for a few drift calculations over a short distance. The Runge-Kutta method solves for the equations of motion given by the macroscopic theory. The Monte Carlo function is a simplified version of the Microscopic function. The Monte Carlo method provides the best balance between accuracy and computational efficiency, and is used to construct a distribution of the anode drift time t_{drift} as a function of the radius to the POCI (x, y) , as shown in Figure 4.2.

It is evident that the presence of the guard wires and the cuboid geometry of the cell imposes a significant azimuthal dependence upon the relationship between the drift time and the radius of the POCI, particularly for radii greater than 1.5 cm from the wire. In a first attempt at a drift-time model, we naively ignore the azimuthal dependence, and

propose a relation of the form

$$t_{drift} = Ar^B, \quad (4.3)$$

where r is given in mm and t_{drift} in μs . We now consider a segment of the cell described by a sweep centred at the origin of a small angle $d\theta$, with $\mathbf{r} = (r, \theta = 0)$ being defined as a vector pointing along the positive y -axis. The drift time distribution, projected onto the radial axis, of the POCI that lie in this small area dA is better described by the one-to-one fit given in Equation 4.3 than the radial projection of drift times shown in figure 4.2. To extend the model into two dimensions, we apply the fit to each area dA given by $\theta + d\theta$, proceeding clockwise round the cell. This process is repeated twice, first fitting only to radii less than 1.5 cm and secondly for radii in the range $1.5 < r < 2.0$ cm. The result is two pairs of parameters, (A_{close}, A_{far}) and (B_{close}, B_{far}) , whose θ dependence is shown in Figure 4.3.

In the close region, both parameters A and B have been fitted with a function of the form

$$A_{close}, B_{close} = \alpha_{A,B} \cos(\beta_{A,B}\theta) + \gamma_{A,B} \quad (4.4)$$

where α, β, γ are the six separate fit parameters, although the approximation can be made that the period $\beta_A = \beta_B$, reducing the number of required parameters to five. In the far region, a more complicated relation is required, of the form

$$\begin{aligned} A_{far} &= a_A - |b_A \sin(c_A\theta)| - |d_A \cos(2c_A\theta)| - e_A \cos(4c_A\theta) \quad \text{and} \\ B_{far} &= a_B + |b_B \sin(c_B\theta)| + |d_B \cos(2c_B\theta)| + e_B \cos(4c_B\theta) \quad , \end{aligned} \quad (4.5)$$

where a, b, c, d, e are the fit parameters. Once again the period parameter $c_A = c_B$, with the result being that 9 separate parameters must be determined to generate the fit to the region $1.5 < r < 2.0$ cm. The fit does not extend further because the azimuthal dependence

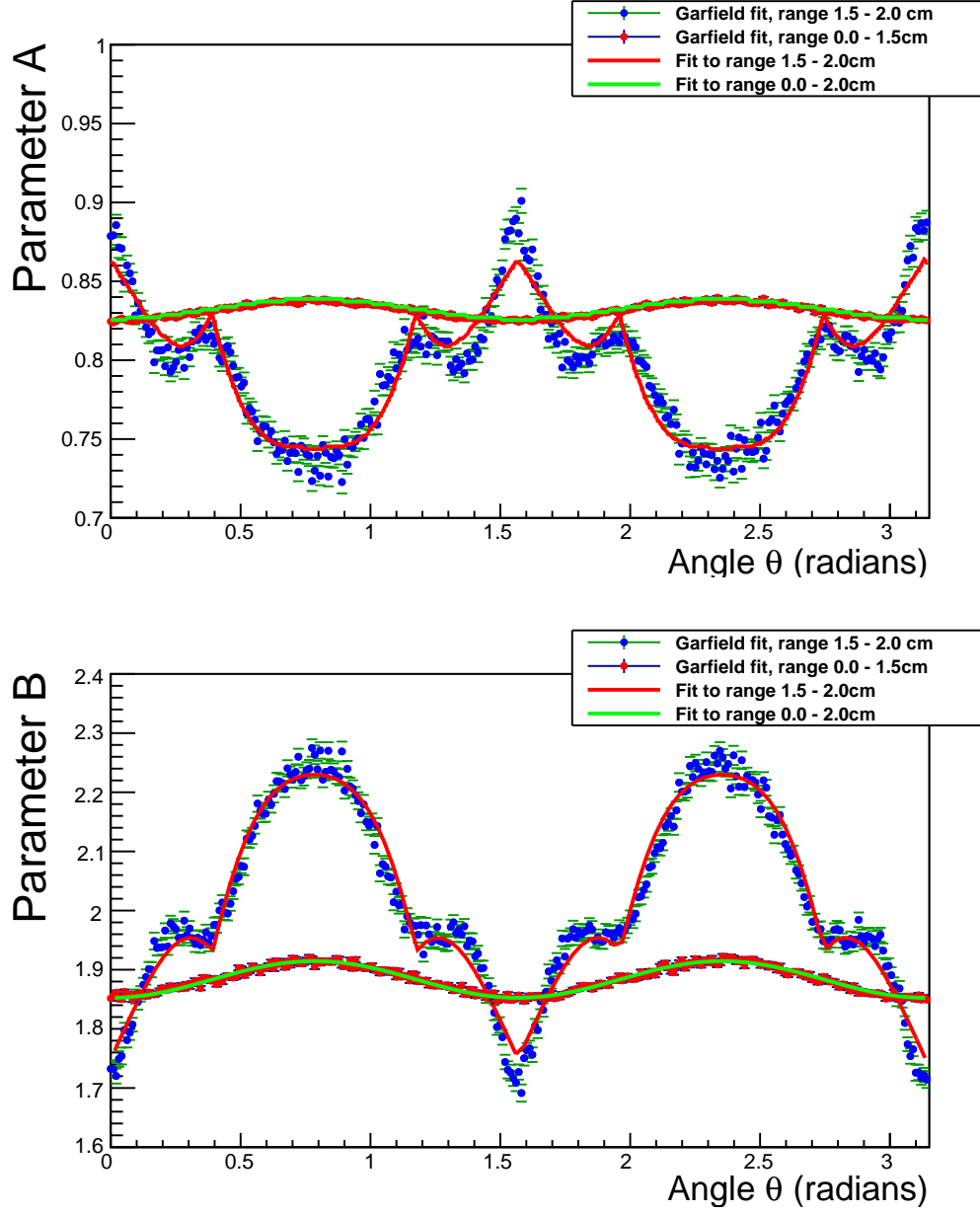


Figure 4.3: Plotting parameters A and B of Equation 4.3 against azimuthal angle θ . The parameters have been fitted with Equation 4.4 for $r < 1.5$ cm and Equation 4.5 for $1.5 < r < 2.0$ cm.

of the parameters at radii greater than 2 cm becomes too convoluted to reliably fit to with any simple function and/or a feasible number of parameters, and so the two-dimensional model in its current form effectively excludes the corners and near edges of the cell.

The result is that the two-dimensional fit model is a combination of two separate drift-time relations, with a total of 14 parameters all dependent upon cell geometry, gas composition and anode voltage. Whilst the geometry is unlikely to change, the gas composition may change during trial runs and the voltages of each cell are likely to be tweaked on a cell-by-cell basis to account for minor differences in construction and cell ageing. The disadvantage of the two-dimensional fit model becomes clear: whenever any change is made to the cell, the fit has to be painstakingly redone to extract the new parameters.

4.2.2 The timemap model

An alternative to the 2D fit introduced in the previous section is to generate a timemap – a one-to-one mapping of (x, y) to t_{drift} – that can then be interpolated to obtain the drift time for a given POCL. The timemap method is implemented as a C++ program that is capable of solving for the potential field in a cell and simulating the drift of electrons from a point in cell until their capture upon the anode wire.

We begin by overlaying the plane of the cell with a fine grid, with each point being given by its coordinate (x_1, y_1) , (x_2, y_2) , etc. The method is composed of two parts: first, we solve for the potential field in the cell, and then we iterate through each point (x_i, y_i) on the grid, calculating the time it takes for an electron cluster generated at this point to reach the anode wire. The resulting collection of locations and times (x_i, y_i, t_i) is the timemap, from which we can determine the drift time at an arbitrary point in the cell (x, y) by using bi-linear interpolation.

The potential field for a cell cross-section is solved via a successive over-relaxation (SOR) method, using a program called CELLSOLVER [43] specially developed for this

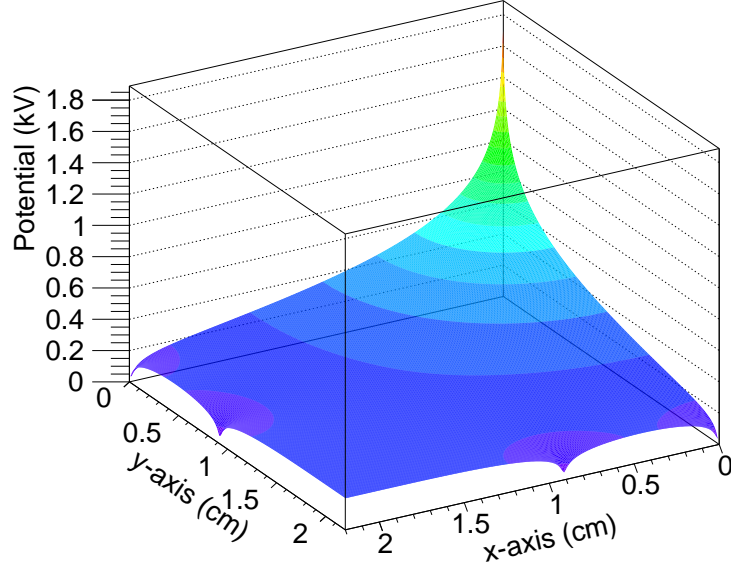


Figure 4.4: The potential field in a SuperNEMO quarter cell operating at 1.7 kV, as determined by the CELLSOLVER program [43].

study. Due to the symmetry of the problem, only a quarter-cell cross-section is considered, with the wires being given as point-like Dirichlet conditions of finite voltage in the solution to Poisson’s equation. The remaining boundaries are considered as Neumann conditions. The resulting potential field map for a cell operating at 1.7 kV is shown in Figure 4.4.

The CELLSOLVER program is capable of solving $\epsilon_0 \nabla^2 U(\mathbf{r}) = \rho$ to a precision of $10^{-6} \cdot U(\mathbf{r})$, where $U(\mathbf{r})$ is the potential at the point \mathbf{r} in the cell, ρ is the charge density and ϵ_0 is the permittivity of free space. The solution for a SuperNEMO quarter cell is identical to that given by the commercial software FlexPDE. Once the potential field map has been generated, the timemap method takes the gradient of the potential field map to create a vector field map of the electric field. From this vector field map we can interpolate the direction and magnitude of the electric field at any point in the quarter cell.

The MAGBOLTZ program is then used to generate a relation between the electron drift velocity and electric field; this is shown in Figure 4.5. The plateau at 100-300 V/mm is a result of the energy dependence of the cross-sections of Helium, Neon and Ethanol.

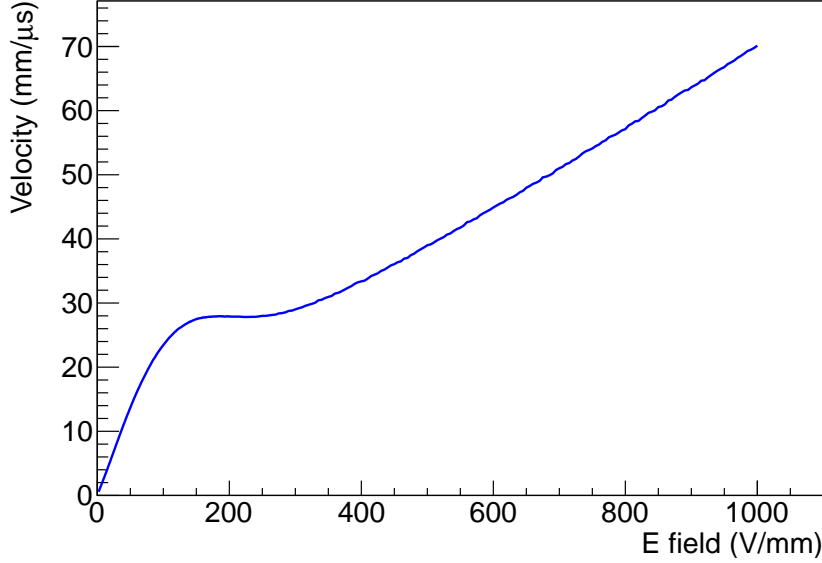


Figure 4.5: The drift velocity to electric field relation as calculated by MAGBOLTZ. The gas mixture is He/Ne/C₂H₅OH in a ratio of 94/2/4% by volume.

We interpolate from this relation to obtain the drift velocity at a given electric field. With the electric vector field map from the CELLSOLVER program and the velocity-field relation from MAGBOLTZ, we simulate the electron drift towards the anode wire for each point (x_i, y_i) on the grid. This is done using an improved Euler two-step method, starting from the point (x_i, y_i) and ending on the surface of the wire, with each step being made using

$$\mathbf{r}'_{n+1} = \mathbf{r}_n + \frac{1}{2}(\mathbf{u}_n + \mathbf{u}_{n+1}) dt, \quad (4.6)$$

where \mathbf{u}_n is the drift velocity at step n corresponding to an electric field \mathbf{E} at the point \mathbf{r}_n and dt is a small time step. An improved Euler method was chosen over the more accurate fourth-order Runge-Kutta due to being more computationally efficient. Practically, each step is made in two parts. First, the velocity at the point \mathbf{r}_n is calculated and the step performed according to the simpler Euler step-wise method, i.e. that $\mathbf{r}_{n+1} = \mathbf{r}_n + \mathbf{u}_n dt$. The velocity \mathbf{u}_{n+1} is calculated at the new location and the step is then undone, being

redone using the average being \mathbf{u}_n and \mathbf{u}_{n+1} . Hence, the new location \mathbf{r}'_{n+1} is not the “true” position corresponding to the velocity \mathbf{u}_{n+1} but rather an improved step calculation given by the foreknowledge of the latter. Being a second-order method, the error in each step is on the order of dt^3 , and to avoid excessively large steps in regions of high field (such as in the proximity of the wire) the step size $d\mathbf{r}$ is constrained to a value of half the wire thickness, and the step time $dt = d\mathbf{r}/\mathbf{u}_n$. Furthermore, the step time itself is constrained such that if $d\mathbf{r}/\mathbf{u}_n > dt_{limit}$, the method forces $dt = dt_{limit}$, where dt_{limit} is a user-defined limit on the time step.

Equation 4.6 does not explicitly account for diffusion, which is important in regions of low electric field where the rms displacement due to diffusion is on the order of the drift velocity. To implement this into the drift we consider the movement associated with the two separate diffusion coefficients D_L and D_T introduced in section 3.2.2. The spread of an electron cluster along an axis is described by a Gaussian with a standard deviation as given in Equation 3.16. Thus, to calculate the effect of diffusion, we consider the movement of the edge of the cluster that is closest to the wire. With every step of Equation 4.6 we consider the diffusion from the point on this edge in the direction of the wire. Given this, the drift due to diffusion in the direction of the wire after a time step dt is

$$d\mathbf{r}^{(D)} = \left(2\sqrt{2D_L dt} \cos(\theta) + 2\sqrt{2D_T dt} \sin(\theta) \right) \hat{\mathbf{r}}_n , \quad (4.7)$$

where $\hat{\mathbf{r}}_n$ is the unit vector in the direction of the position vector relative to the wire \mathbf{r}_n and θ is the angle between $\hat{\mathbf{r}}_n$ and \mathbf{E} at the point \mathbf{r}_n . When the magnitude of the electric field falls below a user-specified threshold, the step is made using a modified version of Equation 4.6, given as

$$\mathbf{r}'_{n+1} = \mathbf{r}_n + \frac{1}{2} (\mathbf{u}_n + \mathbf{u}_{n+1}) dt - \frac{1}{2} \left(d\mathbf{r}_n^{(D)} + d\mathbf{r}_{n+1}^{(D)} \right) . \quad (4.8)$$

The choice of the electric field below which the diffusion Equation 4.8 is used is deter-

mined primarily by the ratio $d\mathbf{r}_n^{(D)}/\mathbf{u}(\mathbf{E})_n dt$ and by the value of the electron anisotropy; both can be determined using the MAGBOLTZ program. Alternatively, the simulation can be run with the diffusion Equation 4.8 being used at all electric fields.

An alternative approach to including diffusion is to use Equation 4.6 only when the step size due to the electric field in the direction of the wire is greater than the step size due to the diffusion, i.e. $-\hat{\mathbf{r}} \cdot \mathbf{u}_n dt > d\mathbf{r}_n^{(D)}$. When this is not the case we make the step using only the drift due to diffusion, such that

$$\mathbf{r}'_{n+1} = \begin{cases} \mathbf{r}_n - \frac{1}{2} \left(d\mathbf{r}_n^{(D)} + d\mathbf{r}_{n+1}^{(D)} \right) & \text{if } -\hat{\mathbf{r}} \cdot \mathbf{u}_n dt < d\mathbf{r}_n^{(D)} \text{ and} \\ \mathbf{r}_n + \frac{1}{2} (\mathbf{u}_n + \mathbf{u}_{n+1}) & \text{otherwise.} \end{cases} \quad (4.9)$$

To summarise, we have four options available to us when using the timemap model: no diffusion (exclusively Equation 4.6), diffusion below a user-defined electric field (Equations 4.6 and 4.8), diffusion at all fields (exclusively Equation 4.8) and diffusion being considered separately from the drift due to electric field (Equation 4.9). Of these four, the one most in agreement with an equivalent timemap generated using GARFIELD is the method using Equation 4.9. The timemap generated using Equation 4.9 is shown in Figure 4.6 (a) and the equivalent timemap generated using GARFIELD is shown in Figure 4.6 (b). Figure 4.6 (c) shows the absolute difference between the GARFIELD value and the timemap model, given as a percentage of the GARFIELD value; it is reassuring to see that for most of the quarter cell, the two agree to within 10%. A timemap generated using the two-dimensional fit model is shown in Figure 4.6 (d).

In the presence of a magnetic field, we rely on Tonk's theorem as discussed in section 3.2.2 to model the electron drift without having to regenerate the MAGBOLTZ input. We assume that over a step $d\mathbf{r}$ the mean time τ between collisions is constant, and that the electric field is orthogonal to the magnetic field. The direction of the drift velocity is given by equation 3.14 and its magnitude by

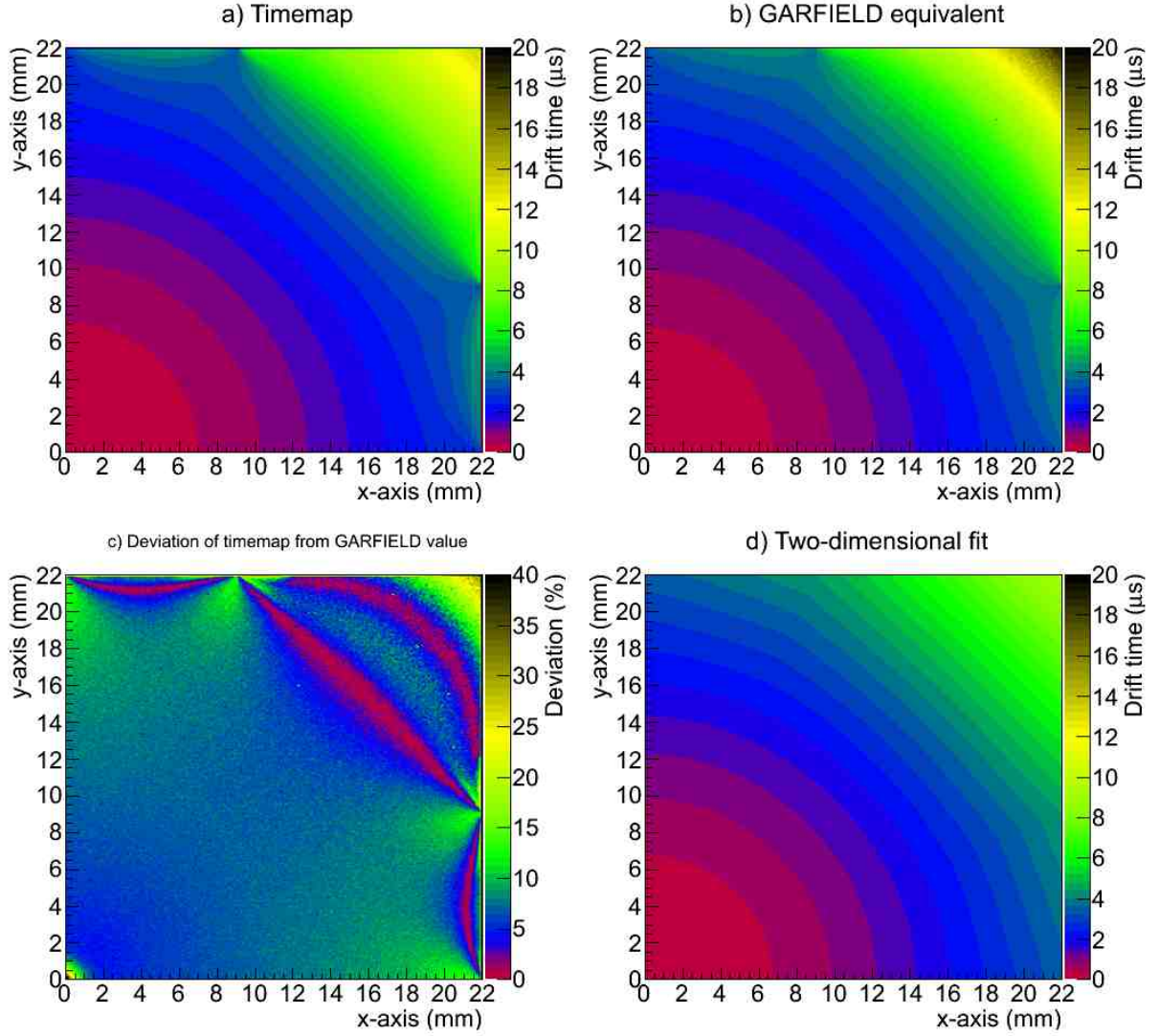


Figure 4.6: Figure (a) shows the timemap for a SuperNEMO quarter cell using the He/Ne/Alcohol mixture, and Figure (b) shows an equivalent timemap generated using GARFIELD. Figure (c) shows the deviation of the timemap from GARFIELD as a percentage of the GARFIELD value. Figure (d) shows a timemap generated using the two-dimensional fit.

$$|\mathbf{u}| = |\mathbf{u}_B| \cos(\phi) , \quad (4.10)$$

where \mathbf{u}_B is the magnitude of the drift velocity in the absence of a magnetic field. The step is then made using this modified drift vector.

In terms of computational efficiency, the timemap in figure 4.6 took 16 minutes 45 seconds to generate on one core of a 64-bit Intel Core 2 Duo at 1.86 GHz, compared to the GARFIELD timemap which took 17 minutes 50 seconds on a 32-bit Intel Pentium M at 1.86 GHz. The efficiency of the timemap model can be further enhanced by enabling the dual-step method, in which a longer step size is used for steps greater than a user-defined radius from the wire, shrinking to a smaller step size once the step enters this radius. It is also possible to load a CELLSOLVER field solution generated earlier directly into the timemap program, reducing the previous calculation to 15 minutes 28 seconds. Once generated, extracting N values from the timemap takes a linearly proportional time $t \propto N$, as it is simply an interpolated lookup table.

We can thus conclude that the timemap model, particularly that which uses Equation 4.9, is the most effective in replicating the drift times given by GARFIELD. Aside from at the corners of the cell, the two agree to within a deviation of 10% from the GARFIELD value and are of comparable computational efficiency. The timemap model is more effective than the two-dimensional fit model since it does not require that the input data from third-party programs be regenerated when the voltage or geometry changes, and can also account for the presence of a magnetic field without having to regenerate the input from MAGBOTLZ.

4.3 Resolution of the simulated drift time

Both the two-dimensional fit and the timemap model are one-to-one relations – two separate events in the simulation with the same POCI will give the same drift time. To account for

the resolution in the drift times that arises due to random fluctuations, the interpolated time given by the models must be smeared using a Gaussian probability distribution with some position-dependent standard deviation.

Equation 3.20 provides a relation for the transverse resolution, but at second glance may prove to be an incorrect choice. The resolution is, in the case of the simulation, inversely proportional to the length of the track through the cell; a glancing track passing through the corner of the cell and the comparatively longer drift distance provides more scope for random fluctuations than the longer track associated with a path passing very close to the anode wire. A GARFIELD Monte Carlo simulation shows that for a given radius r from the anode, the distribution of drift times associated with the ring r to $r + dr$ is well described by a Gaussian of mean t_{drift} and standard deviation σ_t , with the standard deviation increasing with r . At radii beyond $r = 1.4$ cm the electric field loses azimuthal symmetry, and the Gaussian distribution changes into a superposition of Gaussians, each one associated with an angular area $\theta + d\theta$. Although a two-dimensional extrapolation of the resolution is a possibility, in the same manner as was done for the drift time in section 4.2.1, for the sake of simplicity we use a one-dimensional relation fitted to those Gaussians for which $r < 1.4$ cm. The values of σ_t taken from the GARFIELD data and the subsequent fit to these are shown in Figure 4.7.

The result is that for a helium/neon/alcohol mixture in the ratio 94/2/4 percent by volume, the resolution associated with a drift time t_{drift} given by either of the models is

$$\sigma_t = 0.0017 + 0.0166 t_{drift} \quad (4.11)$$

where σ_t and t_{drift} are given in μs .

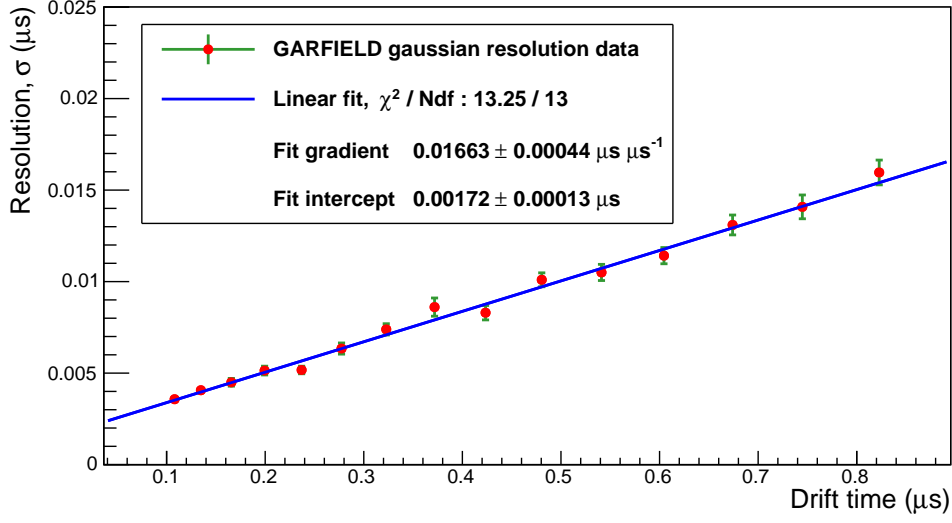


Figure 4.7: Standard deviations of the Gaussians used to fit the distribution of drift times at a given radius, using the GARFIELD Monte Carlo, as a function of drift time.

4.4 Implementation into the simulation software

In this section we will briefly summarise the software utilised throughout this study, and how the timemap and two-dimensional fit models are implemented the simulation. Of greatest importance to simulating the SuperNEMO experiment is the SNWARE software chain, which consists of the software packages Cadfael, Channel, Bayeux and Falaise. In addition to these, the electron drift simulations MAGBOLTZ and GARFIELD are used alongside the specially developed software packages TIMEMAP and CELLSOLVER.

To avoid having to run the SNWARE simulation each time the models are tested, both the timemap model and the two-dimensional fit model have been developed as C++ classes for use either in an SNWARE module or a stand-alone program; in this study they are used in the latter incarnation. A distribution of POCI is generated by running SNWARE and extracting the POCI from each event. A drift time distribution is then constructed by applying the timemap or two-dimensional fit model to each one of the POCI obtained from SNWARE.

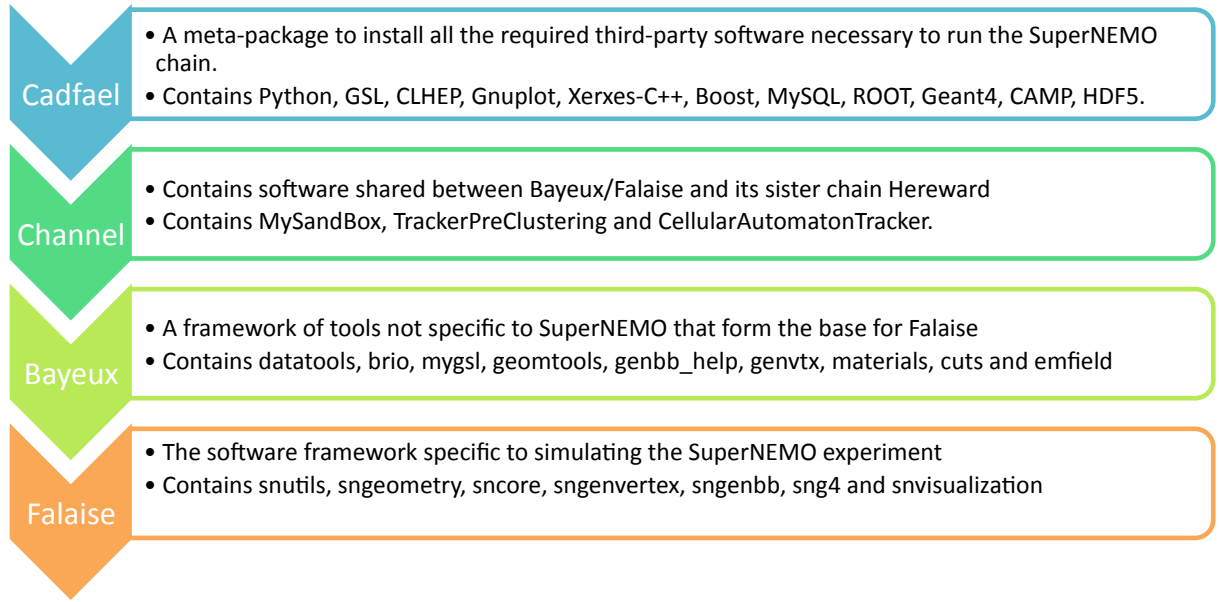


Figure 4.8: The structure of the SNWARE software chain, correct as of 29/06/2012. Each package is dependent upon the one above it.

4.4.1 Structure of the simulation software SNWARE

The SNWARE [44] software chain is a series of software packages intended to simulate the entirety of the SuperNEMO experiment and to analyse the output, both from the simulation and from the real data collected by the future experiment. The software chain comprises four separate parts – Cadfael, Channel, Bayeux and Falaise – whose components and major function are summarised in Figure 4.8.

Cadfael serves as an aggregator package, installing on the user’s system the collaboration-approved versions of the necessary third-party software. The Channel package contains software common to both the Bayeux/Falaise packages and to SNWARE’s sister software chain Hereward, which is used in NEMO3 analyses. Bayeux is a series of general-purpose software packages developed for use at LPC Caen, capable of dealing with data input/output (datatools/brio), geometry management (geomtools/materials) and vertex generation (genvtx/genbb_help). This forms the framework for Falaise, whose packages are specially designed to simulate the SuperNEMO experiment – although they can be

adapted to arbitrary geometries. The particle simulation itself is done using GEANT4 via the `sng4` module. In addition, when the simulation is run, the user has the option of loading custom-built modules into the simulation for various purposes; an example is the `ROOTIO` module, that saves each event as it occurs into a ROOT file suitable for easy analysis at a later date. The software chain is still undergoing development, so the reader is cautioned that this information may not be up-to-date.

4.4.2 Supplementary programs

In addition to the SNWARE software chain, four further software packages are used throughout this study; these are MAGBOLTZ [37], GARFIELD [42], CELLSOLVER [43] and TIMEMAP. MAGBOLTZ simulates the drift of electrons in arbitrary gas mixtures under the influence of electric and/or magnetic fields by solving the Boltzmann equation; the output is used in both the GARFIELD and TIMEMAP packages. The output includes the drift velocity (separate values for x , y and z), the diffusion coefficient (both parallel and transverse to the electric field) and the electron energy distribution for a specified electric field. To obtain the drift velocity to electric field relation required by both GARFIELD and TIMEMAP, MAGBOLTZ must be run for a range of electric fields.

GARFIELD simulates particle drift chambers in 2 or 3 dimensions, using interfaces to both MAGBOLTZ and HEED [45]. The latter serves to simulate the initial ionisation in the chamber due to a traversing particle, and is not used in this study in lieu of the mechanism described in section 3.2.1. GARFIELD can solve for arbitrary electric and magnetic fields in two dimensions, but not to great accuracy; instead, the software relies on importing field solutions from commercial software such as ANSYS Maxwell.

CELLSOLVER [43] and TIMEMAP are packages specially developed for this study. CELLSOLVER solves for the electric field in a SuperNEMO quarter cell using a successive over-relaxation (SOR) method, with the user specifying the voltage on the anode wire and the

number and location of the guard wires. The `CELLSOLVER` code has been incorporated into the `TIMEMAP` package, which is a C++ class designed to simulate the electron drift towards the anode in a SuperNEMO cell, using the timemap model described later in section 4.2.2.

Chapter 5

Comparison of the models to experimental data

In this chapter we compare the results of a simulation done using both the two-dimensional fit model and timemap interpolation against data taken using a SuperNEMO 18-cell module in use at the University of Manchester. The SNWARE simulation has been adapted to reflect the geometry and physics of the 18-cell module, which is coupled to a photomultiplier tube (PMT) that serves as the event trigger.

5.1 The SuperNEMO 18-cell module

The 18-cell module is 9 cells wide by 2 cells deep and kept in a sealed tank that contains the gas mixture. Placed directly on top of the tank, vertically in line with the central cell, is a scintillator with an attached PMT that serves as a trigger for an event. The anodes of each cell are connected directly to an analogue-to-digital converter (ADC). Unlike previous prototype cells, the derivative signal is not taken; instead, this is calculated later during analysis. The cathode signals are not used during this experiment and hence are not connected to the ADC. A simplified schematic of the setup is shown in Figure 5.1.

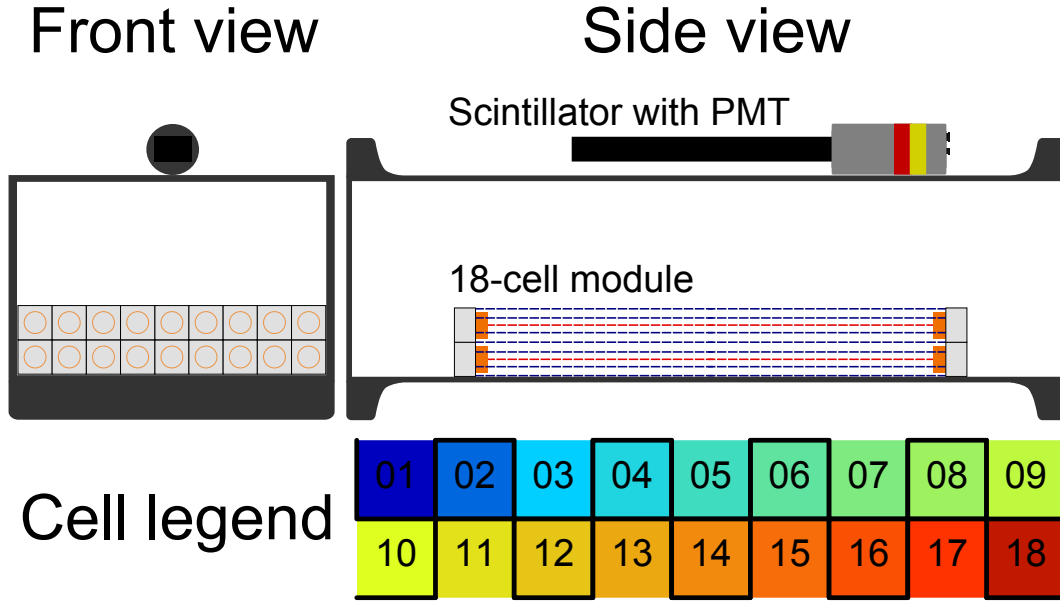


Figure 5.1: A simplified diagram of the experimental setup, and the cell numbering as used in this study.

The cell numbering that will be used is shown in Figure 5.1. The acquisition triggers on the passage of a particle through the PMT and any one of cells 02 to 08. The PMT signal is passed through a gate unit before connecting to the ADC. Any signal from one of the aforementioned cells within a $35 \mu\text{s}$ window following the PMT signal is registered as a coincidence and saves the event to file.

An uninterrupted data run of 29,400 events was taken over the course of 20 hours, with each cell operating at 1.7 kV and the PMT at 1.8 kV. The gas mixture the cell was helium/neon/alcohol in the ratio 94/2/4 percent by volume, at room temperature and pressure. The collected data is passed through an analysis program that applies the following criteria:

1. Cell 14 must have fired.
2. $t_{\text{anode}} > t_{\text{pmt}}$, where t_{anode} and t_{pmt} are the time a signal was detected on the anode and PMT, respectively.

3. The pedestal voltage must be greater than 760 mV and less than 800 mV.
4. Either cell 04, 05 or 06 must have fired.
5. No cells other than 04, 05, 06, 13, 14 and 15 must have fired.
6. The time t_{pmt} must be $48\mu < t_{pmt} < 52\mu s$.
7. If cell 04 fired, cell 06 must not have fired, and viceversa.

The requirement that $48 < t_{pmt} < 52 \mu s$ is because the trigger signal, by the settings on the ADC, should lie at $t = 50 \mu s$ in the event window.

Out of 28,400 events, 3207 fulfill the criteria. From these events, we take the drift time to be $t_{drift} = t_{anode} - t_{pmt}$. To remove background events due to random coincidences, we make a linear fit to the region 30 to 59 μs in the drift time distribution and remove from each bin the value of the offset given by the fit. The drift time distribution extracted from the data (both with and without background removed) is shown in Figure 5.2.

5.2 Applying the models

To simulate the experimental setup, a special SNWARE run was made with a modified geometry to mimic that in Figure 5.1. A single SuperNEMO cell is located within a tank, placed directly beneath a block serving as the scintillator trigger. Cosmic muons, in a ratio μ^+/μ^- of 1.2, are generated directly above the scintillator block, with an energy distribution described by a Gaussian of mean 4 GeV and standard deviation 1 GeV. Each particle is generated pointing downwards toward the cell, with a momentum vector lying within a cone of 70° . The zenith of the particle's direction is described by a probability distribution function of shape $\cos^2 \theta$. If the particle enters the drift cell, ionisation clusters are generated along its track in the manner described in section 3.2.1. The POCI of each

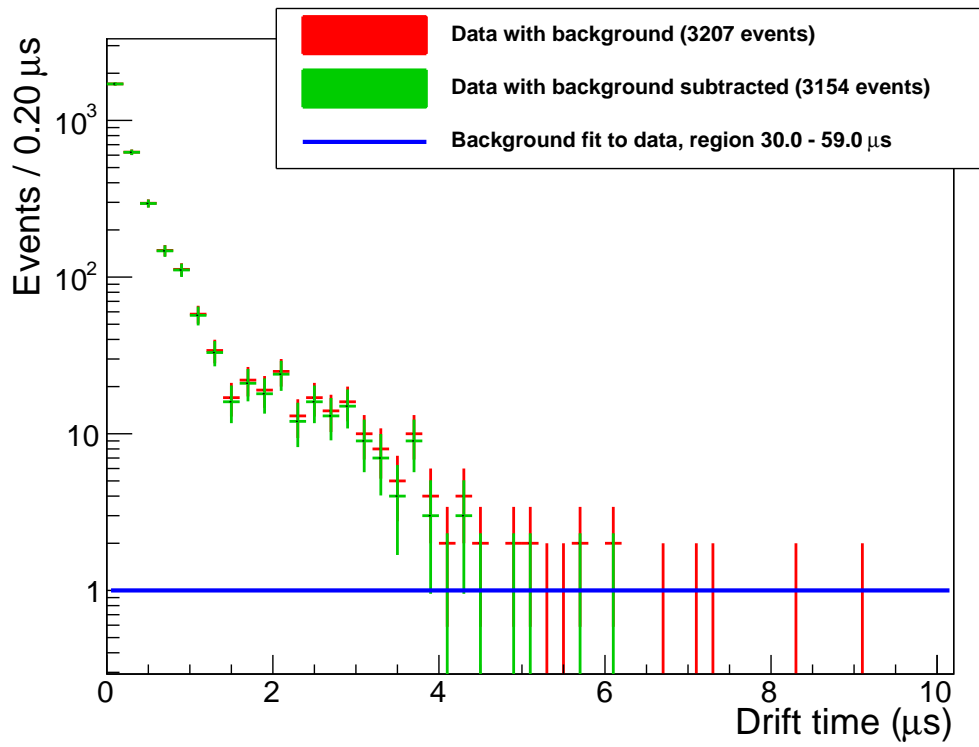


Figure 5.2: The drift time distribution extracted from the 18-cell data, with and without background subtraction.

event are used to build a distribution of POCI to which we will then apply the drift time models.

We apply the two models to each POCI in the distribution generated by the simulation to obtain a distribution of drift times. For the timemap model, the effects of diffusion are considered in three separate stages; no diffusion, diffusion being separate from electric field (as used in Equation 4.9), and diffusion at all fields. The resulting four sets of simulation drift times are shown plotted against the drift time distribution from Figure 5.3. Each distribution has been normalized to represent a distribution due to 10,000 events.

The timemap model with diffusion considered separately agrees with the two-dimensional fit model to within a deviation of 20% from the timemap drift time distribution for drift times up to $2.2 \mu\text{s}$. However, neither model describes the excess of short drift times seen in the data, nor the comparative absence of data with drift times greater than $8 \mu\text{s}$. Since the timemap model produces similar results to those of the two-dimensional fit (and, as seen in Figure 4.6, GARFIELD), it is possible that the distribution of POCI generated by the simulation is incorrect.

When considering the individual components of the simulation, the timemap model has already been shown to agree with GARFIELD to within a percentage deviation of 10% from the GARFIELD drift time. Furthermore, the model used to generate cosmic ray muons in the simulation, although simplified, is unlikely to be inaccurate enough to account for the discrepancy. The cuts made in section 5.1 ensure that the drift time distribution in Figure 5.3 results only from events where a single particle descended through the PMT and then triggered the cell, so the simulation geometry and particle generation should be an accurate representation of the physics. This leads us to conclude that the discrepancy is due to an inaccuracy in how the ionisation process is simulated and the resulting POCI are generated. In the next section we will investigate to what degree a re-distribution of the POCI can affect the outcome of the simulation.

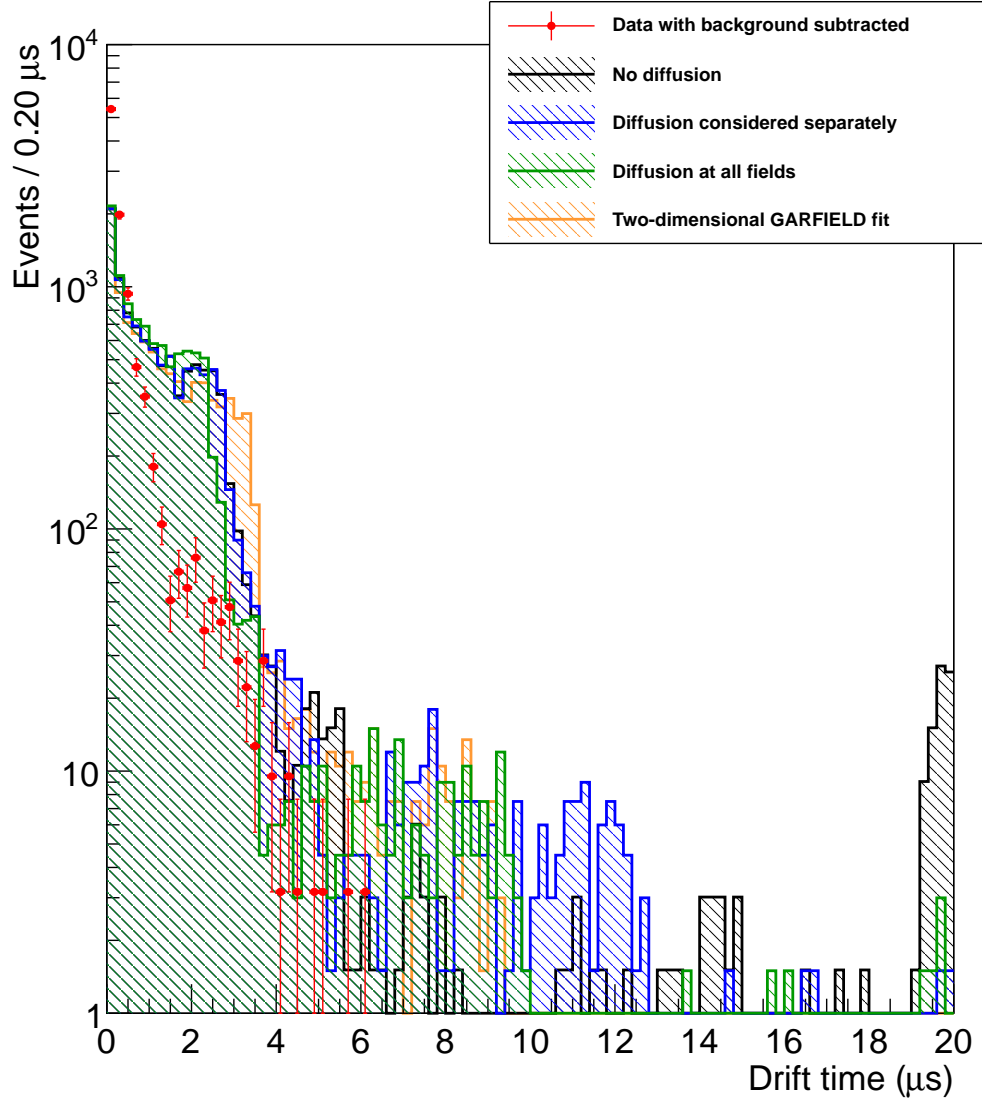


Figure 5.3: The timemap model and GARFIELD two-dimensional fit against the drift time distribution extracted from the 18-cell data. The distributions have been normalized to represent a total of 10,000 events

5.3 Re-distributing the POCI

The distribution of POCI generated with the SNWARE simulation, which uses the ionisation process described in section 3.2.1, is shown in Figure 5.4 (a). In an attempt to reconcile the simulation with the data, we generate a new distribution using a random number generator [46] and separate probability density functions for the x and y axes.

We generate each POCI by separately sampling its x and y coordinate from a probability density function (PDF). The PDF for the y -coordinate is given by a Gaussian with a standard deviation of 0.1 cm, while the PDF for the x -coordinate is a Gaussian with a standard deviation of 0.58 cm and a linear offset. The generator does not allow POCI to be generated inside or within 40 microns of the wire. This combination of PDFs was chosen because it supposes that the ionisation process described in section 3.2.1 is largely correct but that the electrons generated at the POCI of radius greater than 0.5 cm are less likely to reach the anode wire due to some unknown factor. A distribution of 10,000 POCI generated using these PDFs is shown in Figure 5.4 (b).

We apply the timemap and two-dimensional fit models to the new distribution of POCI in Figure 5.4 to obtain a set of four drift time distributions. This new set of drift times is plotted against the data in Figure 5.5. Once again, the distributions have been normalized to represent a distribution due to 10,000 events.

With the re-distributed POCI the simulation is a far better match to the data than was seen in Figure 5.3; this appears to confirm that the discrepancy is due to an inaccuracy in the ionisation process that the simulation uses to generate the POCI. Whether this hypothesis is correct, and what modifications will have to be made to the ionisation process if it is, are the scope for future work.

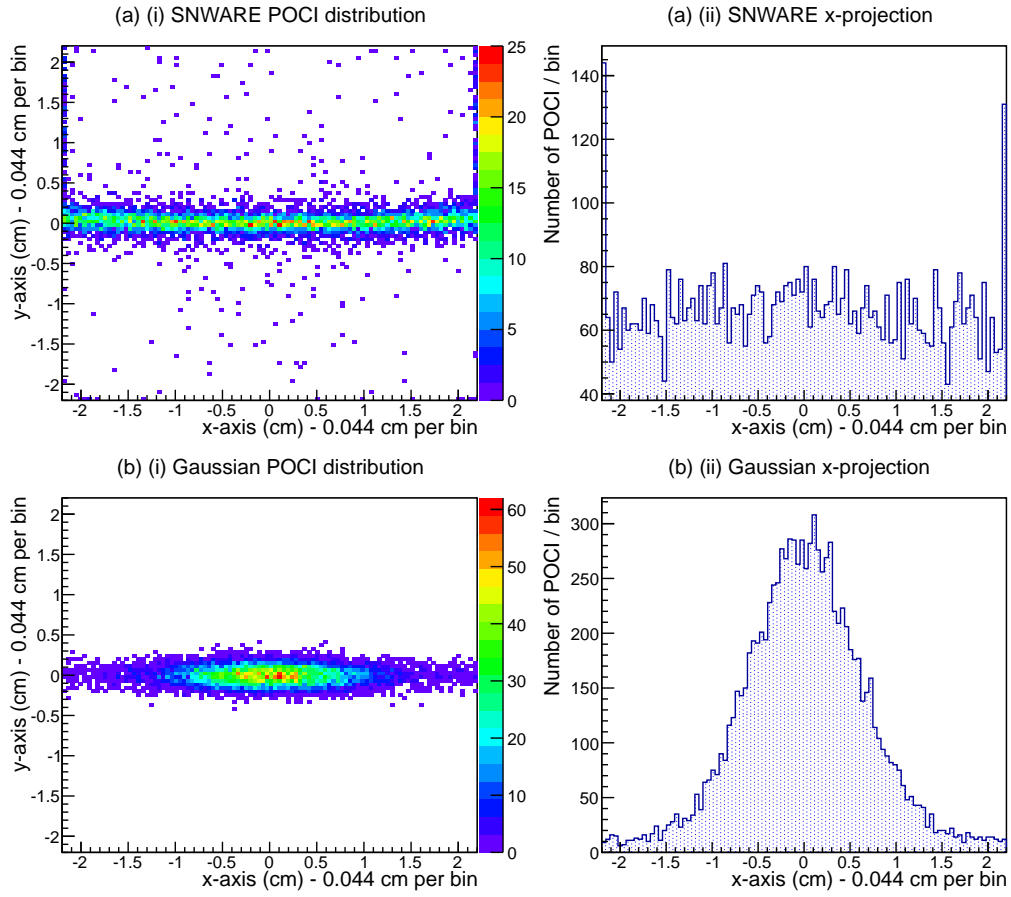


Figure 5.4: The distribution of POCI in the cell, as given by (a) the SNWARE simulation and (b) the probability density functions on the x and y axes as given in Section 5.3

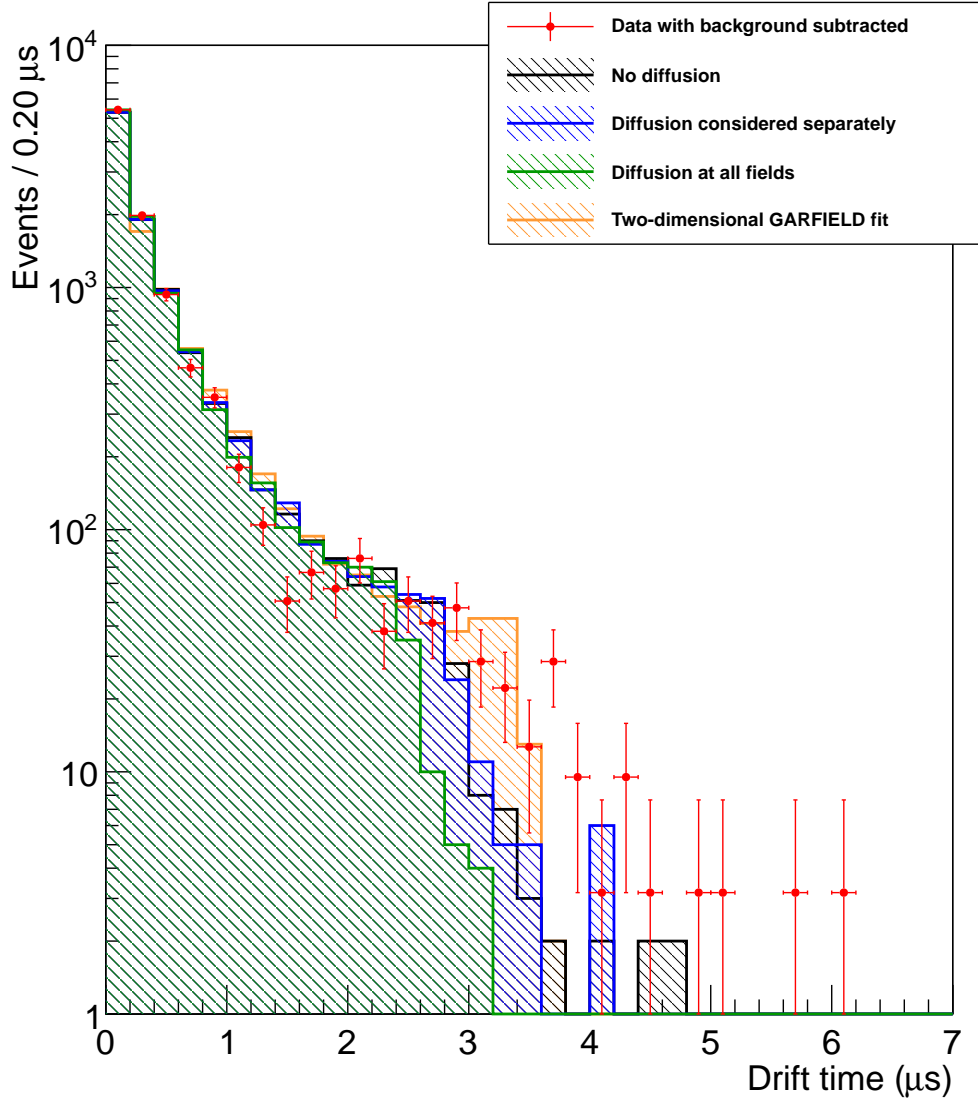


Figure 5.5: The drift time distributions for the timemap and two-dimensional fit models, generated using the distribution of POCI in Figure 5.4 (b), against the drift time distribution extracted from the 18-cell data. The distributions have been normalized to represent a total of 10,000 events.

Chapter 6

Conclusion

To develop an accurate simulation of the SuperNEMO experiment, an accurate description of the Geiger cells that constitute the tracker volume is necessary. In this study we have examined both the cathode and anode response of a Geiger cell, and compared simulations of the anode response to data.

Data collected using a SuperNEMO prototype cell has shown that the linear relation between the longitudinal coordinate of the point of closest ionisation (POCI) and the cathode relation used in the NEMO3 experiment is appropriate for use in SuperNEMO. Recovery effects from previous events increase the plasma propagation time and decrease the probability that the plasma will propagate the entire length of the cell. These effects are important at event delays of less than 5 ms, corresponding to an event rate of 200 Hz. Since the event rate per cell in SuperNEMO is expected to be ≈ 0.05 Hz, the effects of cell recovery are unlikely to require consideration in the simulation.

To simulate the drift of the ionisation from the POCI to the anode wire under the influence of the electric field, two models have been developed as part of this study; the timemap model and the two-dimensional fit model. Both these models have been implemented as C++ software packages that can be run as part of, or separate from, the SuperNEMO simulation software.

Of the two models introduced to simulate the drift of the ionisation from the POCI to the anode wire, the timemap model shows the greatest similarity to an equivalent simulation done with GARFIELD. The timemap model where drift due to diffusion is considered separately from drift due to the electric field is compared with an equivalent GARFIELD timemap. This is done by taking the absolute difference between the drift time interpolated from the timemap and GARFIELD, and dividing it by the GARFIELD drift time to obtain the percentage deviation from GARFIELD. Drift times interpolated from the timemap deviate no more than 10% from the GARFIELD drift time for radii less than 2.2 cm. However, the different treatment of regions of low electric field and the geometry of the wires increases the deviation from the GARFIELD drift time to a maximum of approximately 40% in the corner regions and in close proximity of the guard wires.

Although the two-dimensional fit model is the most computationally efficient of the two models, the timemap model shows similar computation times to GARFIELD when using equal processing power, with the potential for greater efficiency than GARFIELD if the step size is increased in regions far from the anode wire. The timemap also has an advantage over GARFIELD in that, having been implemented in C++ as opposed to FORTRAN, it can be implemented directly into the SuperNEMO software simulation SNWARE.

Comparison to data taken with the 18-cell module shows that the timemap and two-dimensional fit models produce similar distributions of drift times, agreeing to within 20% of the timemap value for drift times less than $2.4 \mu\text{s}$. This corresponds to a distance of less than 1.7 cm from the anode. However, initial simulations using the ionisation model already present in the SNWARE chain demonstrate an excess of events at short drift times in the data compared to both the timemap and two-dimensional fit models. This is rectified by altering the distribution of POCI generated by the ionisation model, following which the drift time distribution generated by the timemap model agrees to the data within

an average deviation of 28% from the data value. The much improved agreement suggests that the method used to simulate the ionisation that occurs during the passage of a charged particle through the cell is inaccurate; whether this hypothesis is correct is the scope for future work.

References

- [1] D. Griffiths, *Introduction to Elementary Particles*. Wiley-VCH, 2009.
- [2] C. L. Cowan, Jr., F. Reines, F. B. Harrison, H. W. Kruse, and A. D. McGuire, “Detection of the Free Neutrino: A Confirmation,” *Science*, vol. 124, pp. 103–104, July 1956.
- [3] Wikimedia, “Standard model of elementary particles.” Licensed under Creative Commons 3.0.
- [4] K. Nakamura *et al.*, “Review of particle physics,” *J.Phys.G*, vol. G37, p. 075021, 2010.
- [5] Y. Fukuda *et al.*, “Evidence for oscillation of atmospheric neutrinos,” *Phys. Rev. Lett.*, vol. 81, pp. 1562–1567, Aug 1998.
- [6] Q. Ahmad *et al.*, “Measurement of the rate of $\nu/e + d \rightarrow p + p + e^-$ interactions produced by B-8 solar neutrinos at the Sudbury Neutrino Observatory,” *Phys.Rev.Lett.*, vol. 87, p. 071301, 2001.
- [7] K. Eguchi *et al.*, “First results from KamLAND: Evidence for reactor anti-neutrino disappearance,” *Phys.Rev.Lett.*, vol. 90, p. 021802, 2003.
- [8] M. Goeppert-Mayer, “Double beta-disintegration,” *Phys. Rev.*, vol. 48, pp. 512–516, Sep 1935.

- [9] M. G. Inghram and J. H. Reynolds, “Double beta-decay of ^{130}Te ,” *Phys. Rev.*, vol. 78, pp. 822–823, June 1950.
- [10] A. Barabash, “Average (recommended) half life values for two neutrino double beta decay,” *Czech.J.Phys.*, vol. 52, pp. 567–573, 2002.
- [11] S. King, *Measurement of the Double Beta Decay Half-Life of ^{100}Mo to the 0_1^+ Excited State, and ^{48}Ca to the Ground State in the NEMO 3 Experiment*. PhD thesis, University College London, October 2008.
- [12] A. Barabash, “Average and recommended half-life values for two neutrino double beta decay: Upgrade-09,” *AIP Conf.Proc.*, vol. 1180, pp. 6–15, 2009.
- [13] R. Arnold *et al.*, “Measurement of the $\beta\beta$ decay half-life of ^{130}Te with the nemo-3 detector,” *Phys. Rev. Lett.*, vol. 107, p. 062504, Aug 2011.
- [14] N. Ackerman *et al.*, “Observation of two-neutrino double-beta decay in ^{136}Xe with the exo-200 detector,” *Phys. Rev. Lett.*, vol. 107, p. 212501, Nov 2011.
- [15] W. Furry, “On transition probabilities in double beta-disintegration,” *Phys.Rev.*, vol. 56, pp. 1184–1193, 1939.
- [16] F. Avignone, R. Brodzinski, *et al.*, “The international germanium experiment (IGEX) in 1993,” *Nuclear Physics B - Proceedings Supplements*, vol. 35, no. 0, pp. 354 – 357, 1994.
- [17] H. Klapdor-Kleingrothaus, “The HEIDELBERG-MOSCOW Ge-76 double beta experiment in Gran Sasso 1990-2003 and status of absolute neutrino mass,” pp. 307–364, 2003.
- [18] E. Previtali, C. Arnaboldi, D. Artusa, F. Avignone, M. Balata, *et al.*, “CUORICINO: A new large bolometer array for astroparticle physics,” *Nucl.Instrum.Meth.*, vol. A518, pp. 256–258, 2004.

- [19] H. Simgen, “Gerda: A new 76Ge double beta decay experiment at gran sasso,” *Nuclear Physics B - Proceedings Supplements*, vol. 143, no. 0, p. 567, 2005.
- [20] L. Ejzak, “The Search for Neutrinoless Double Beta Decay in CUORE,” 2009.
- [21] K. Kume, K. Fushimi, R. Hazama, M. Kawasaki, N. Kudomi, *et al.*, “Double beta decays studied by ELEGANT,” pp. 490–495, 1995.
- [22] R. Arnold, C. Augier, *et al.*, “Technical design and performance of the nemo 3 detector,” *Nuclear Instruments and Methods in Physics Research Section A: Accelerators, Spectrometers, Detectors and Associated Equipment*, vol. 536, pp. 79 – 122, 2005.
- [23] R. Arnold, C. Augier, *et al.*, “First results of the search for neutrinoless double-beta decay with the nemo 3 detector,” *Phys. Rev. Lett.*, vol. 95, p. 182302, Oct 2005.
- [24] J. Argyriades *et al.*, “Measurement of the Double Beta Decay Half-life of Nd-150 and Search for Neutrinoless Decay Modes with the NEMO-3 Detector,” *Phys.Rev.*, vol. C80, p. 032501, 2009.
- [25] H. Klapdor-Kleingrothaus, A. Dietz, L. Baudis, G. Heusser, I. Krivosheina, *et al.*, “Latest results from the Heidelberg-Moscow double beta decay experiment,” *Eur.Phys.J.*, vol. A12, pp. 147–154, 2001.
- [26] H. Klapdor-Kleingrothaus, “Status of evidence for neutrinoless double beta decay, and the future: GENIUS and GENIUS TF,” pp. 263–282, 2003.
- [27] C. Aalseth, I. Avignone, F.T., A. Barabash, F. Boehm, R. Brodzinski, *et al.*, “Comment on ‘Evidence for neutrinoless double beta decay’,” *Mod.Phys.Lett.*, vol. A17, pp. 1475–1478, 2002.
- [28] R. Arnold *et al.*, “Probing New Physics Models of Neutrinoless Double Beta Decay with SuperNEMO,” *Eur.Phys.J.*, vol. C70, pp. 927–943, 2010.

- [29] W. Blum and L. Rolandi, *Particle Detection with Drift Chambers*. Springer-Verlag, 1994.
- [30] F. Mauger. Internal communications.
- [31] G. collaboration, *GEANT4*. version 9.4.04, April 2012.
- [32] A. Peisert and F. Sauli, *Drift and diffusion of electrons in gases: a compilation (with an introduction to the use of computing programs)*. Geneva: CERN, 1984.
- [33] L. Tonks, “Particle transport, electric currents, and pressure balance in a magnetically immobilized plasma,” *Phys. Rev.*, vol. 97, pp. 1443–1445, Mar 1955.
- [34] E. B. Wagner, F. J. Davis, and G. S. Hurst, “Time-of-Flight Investigations of Electron Transport in Some Atomic and Molecular Gases,” *J. Chem. Phys.*, vol. 47, pp. 3138–3147, Nov. 1967.
- [35] K. F. Ness, “Spherical-harmonics decomposition of the boltzmann equation for charged-particle swarms in the presence of both electric and magnetic fields,” *Phys. Rev. E*, vol. 47, pp. 327–342, Jan 1993.
- [36] G. W. Fraser and E. Mathieson, “Monte Carlo calculation of electron transport coefficients in counting gas mixtures I. Argon-methane mixtures,” *Nuclear Instruments and Methods in Physics Research A*, vol. 247, pp. 544–565, July 1986.
- [37] S. Biagi, *MAGBOLTZ*. version 9.0.1, May 2012.
- [38] R. L. Flack. Internal communications.
- [39] T. Lee. Internal communications.
- [40] C. Augier, R. Arnold, *et al.*, “Technical performance of the NEMO 3 detector ”Advantages and limitations”, tech. rep., 2005. Corinne AUGIER for the NEMO Collaboration.

- [41] E. Chaveau. Internal communications.
- [42] R. Veenhof, *GARFIELD*. version 9, September 2010.
- [43] D. Teresi, *CellSolver*. version 1.0, November 2011.
- [44] F. Mauger, M. Bongrand, X. Garrido, B. Guillon, Y. Shitov, and F. Nova, *SNWARE software chain*. version 2.0 β , 2012.
- [45] I. Smirnov, *HEED*. version 1.01, March 1997.
- [46] M. Matsumoto and T. Nishimura, “Mersenne Twistor: A 623-dimensionally equidistributed uniform pseudorandom number generator,” *ACM Transactions on Modeling and Computer simulation*, vol. 8, pp. 3–30, January 1998.